Supplemental materials for
Topological state transitions in electromagnetic topological defects

Peng Shi[1,†], Xinxin Gou[1], Qiang Zhang[1], and Xiaocong Yuan[1,2‡]

[1]*Nanophotonics Research Centre, Institute of Microscale Optoelectronics & State Key Laboratory of Radio Frequency Heterogeneous Integration, Shenzhen University, Shenzhen 518060, China*
[2]*Zhejiang Lab, Research Center for Humanoid Sensing, Research Institute of Intelligent Sensing, Hangzhou 311100, China*

Corresponding author: †pittshiustc@gmail.com; ‡*xcyuan@szu.edu.cn*

Contents:

I. Classical Lorentz model of dielectric function

In classical electromagnetic (EM) theory, the wave-matter interactions can be described by the Maxwell's equations [S1]:

$$\begin{gathered}\nabla \cdot \mathbf{D} = 0 \\ \nabla \times \mathbf{E} = -\frac{\partial \mathbf{B}}{\partial t} \\ \nabla \cdot \mathbf{B} = 0 \\ \nabla \times \mathbf{H} = \mathbf{J}_\sigma + \frac{\partial \mathbf{D}}{\partial t}\end{gathered}, \tag{S1}$$

with the constitutive relations in an isotropic medium expressed as

$$\begin{gathered}\mathbf{D} = \varepsilon_0 \mathbf{E} + \mathbf{P} \\ \mathbf{B} = \mu \mathbf{H} \\ \mathbf{J}_\sigma = \sigma \mathbf{E}\end{gathered}. \tag{S2}$$

Here, **D** is electric displacement vector; **E** is the electric field strength; **B** is the magnetic induction strength; **H** is the magnetic field strength; $\mathbf{J}_\sigma$ is the current density; ε_0 is the permittivity of vacuum; **P** is the electron polarization; μ is the magnetic permeability and there is $\mu = \mu_0$ through the manuscript; σ is the electron conductance. We do not consider the free charges $\rho_f = 0$.

Then, we consider the Lorentz model of electric permittivity in medium. The electron gas subjected to an external electric field **E** can be given by [S1]:

$$m_e\left(\ddot{\mathbf{r}} + \gamma \dot{\mathbf{r}} + \omega_i^2 \mathbf{r}\right) = -e\mathbf{E}(t). \tag{S3}$$

Here, **r** is the position vector of electron; m_e is the mass of electron; the electrons oscillate in response to the applied electromagnetic (EM) field $\mathbf{E}(t)$, and their motion is damped with a characteristic frequency $\gamma = 1/\tau$ and τ is the relaxation time of electron gas. We assume that there are diversiform types of electrons, including the free electron and polarized electrons; ω_i is the displacement electron resonance frequency of i-th type electrons and there is $\omega_i = 0$ for the metal materials. If we assume a harmonic time dependence $\mathbf{E}(t) = \mathbf{E}_0 e^{-i\omega t}$ of the driving field (we use this time convention throughout the manuscript and supplementary materials), a solution of this equation describing the oscillation of the electron is

$$\mathbf{r}_i = \frac{e}{m_e} \frac{1}{\left(\omega^2 - \omega_i^2 + i\omega\gamma\right)} \mathbf{E}, \tag{S4}$$

and the velocity is

$$\mathbf{v}_i = \dot{\mathbf{r}}_i = -\frac{e}{m_e} \frac{i\omega}{\left(\omega^2 - \omega_i^2 + i\omega\gamma\right)} \mathbf{E}. \tag{S5}$$

Firstly, for the metal materials, there are $\mathbf{J}_\sigma \neq 0$ and electric polarization $\mathbf{P} = 0$. Thus, the current density is

$$\mathbf{J}_\sigma = -N\sum_i e\mathbf{v}_i = \frac{Ne^2}{m_e} \sum_i \frac{i\omega f_i}{\left(\omega^2 - \omega_i^2 + i\omega\gamma\right)} \mathbf{E} = \sigma \mathbf{E}. \tag{S6}$$

In the special case that there is only one type of free electron, the current can be downgraded into

$$\mathbf{J}_{\sigma} = -Ne\mathbf{v}_{i} = \frac{Ne^{2}}{m_{e}} \frac{i\omega}{\left(\omega^{2} - \omega_{i}^{2} + i\omega\gamma\right)} = \sigma\mathbf{E} \tag{S7}$$

and the fourth equation of Maxwell's equation can be written as

$$\nabla \times \mathbf{H} = \mathbf{J}_{\sigma} + \frac{\partial \mathbf{D}}{\partial t} = -i\omega\left(\varepsilon_{0} + i\frac{\sigma_{\omega}}{\omega}\right)\mathbf{E} = -i\omega\varepsilon_{0}\left(1 - \frac{\omega_{p}^{2}}{\left(\omega^{2} - \omega_{i}^{2} + i\omega\gamma\right)}\right)\mathbf{E} = -i\omega\varepsilon\left(\omega\right)\mathbf{E} = \frac{\partial \mathbf{D}\left(\omega\right)}{\partial t}. \tag{S8}$$

Here, N is the density of free electrons; $\omega_{p} = \sqrt{Ne^{2}/m_{e}\varepsilon_{0}}$ is the plasma frequency and $\omega_{i} = 0$.

On the other hand, for the dielectric materials, there are $\mathbf{J}_{\sigma} = 0$ and electric polarization $\mathbf{P} \neq 0$ ($\mathbf{D} = \varepsilon_{0}\mathbf{E} + \mathbf{P}$). The electric dipole moment $\mathbf{p}$ is

$$\mathbf{p} = -e\mathbf{r} = -\frac{e^{2}}{m_{e}} \frac{1}{\left(\omega^{2} - \omega_{i}^{2} + i\omega\gamma\right)}\mathbf{E}, \tag{S9}$$

and the electron polarization is

$$\mathbf{P} = -\varepsilon_{0} \frac{Ne^{2}}{m_{e}\varepsilon_{0}} \sum_{i} \frac{f_{i}}{\left(\omega^{2} - \omega_{i}^{2} + i\omega\gamma\right)}\mathbf{E} = \varepsilon_{0}\chi_{P}\mathbf{E}. \tag{S10}$$

In the special case that there is only one type of electric dipole moment, the electron polarization can be downgraded into

$$\mathbf{P} = -\varepsilon_{0} \frac{Ne^{2}}{m_{e}\varepsilon_{0}} \frac{1}{\left(\omega^{2} - \omega_{i}^{2} + i\omega\gamma\right)}\mathbf{E} = \varepsilon_{0}\chi_{P}\mathbf{E} \tag{S11}$$

and the fourth equation of Maxwell's equation can be written as

$$\nabla \times \mathbf{H} = \mathbf{J}_{\sigma} + \frac{\partial \mathbf{D}}{\partial t} = -i\omega\left(\varepsilon_{0}\mathbf{E} + \mathbf{P}\right) = -i\omega\varepsilon_{0}\left(1 - \frac{\omega_{p}^{2}}{\left(\omega^{2} - \omega_{i}^{2} + i\omega\gamma\right)}\right)\mathbf{E} = -i\omega\varepsilon\left(\omega\right)\mathbf{E} = \frac{\partial \mathbf{D}\left(\omega\right)}{\partial t}. \tag{S12}$$

Here, $\omega_{p} = \sqrt{Ne^{2}/m_{e}\varepsilon_{0}}$ is consistent with the plasma frequency.

Overall, from the equation (S8) and (S12), no matter for the metal or for the dielectric, the permittivity $\varepsilon(\omega)$ can be expressed universally by

$$\varepsilon\left(\omega\right) = \varepsilon_{0}\left(1 - \frac{\omega_{p}^{2}}{\left(\omega^{2} - \omega_{i}^{2} + i\omega\gamma\right)}\right). \tag{S13}$$

Therefore, the Maxwell's equations and Helmholtz equations of EM field can be expressed as

$$\begin{gathered} \nabla \cdot \mathbf{D}\left(\omega\right) = 0 \\ \nabla \times \mathbf{E} = -\frac{\partial \mathbf{B}}{\partial t} \\ \nabla \cdot \mathbf{B} = 0 \\ \nabla \times \mathbf{H} = \frac{\partial \mathbf{D}\left(\omega\right)}{\partial t} \end{gathered} \tag{S14}$$

and

$$\begin{gathered}\nabla^2\mathbf{E}+k^2(\omega)\mathbf{E}=0\\ \nabla^2\mathbf{H}+k^2(\omega)\mathbf{H}=0\end{gathered},\tag{S15}$$

respectively. Here, $\varepsilon(\omega)$ is a complex value and depends on the EM frequency. Thus, the wavenumber $k^2(\omega) = \omega^2\varepsilon(\omega)\mu = \omega^2\varepsilon(\omega)\mu_0$ is also complex, where the real part of $k(\omega)$ is related to the propagating property and the imaginary part of $k(\omega)$ is related to the attenuation.

II. Optical Dirac equation and spin-orbit couplings of EM fields

To study the spin-orbit couplings (SOCs) in EM field, it needs to introduce the optical Dirac equation. The Dirac equation is a relativistic quantum mechanical one for elementary spin-1/2 particle [54], whereas with the identity for arbitrary two vectors **A** and **B**: $\mathbf{A}\times\mathbf{B} = -i(\mathbf{A}\cdot\hat{\mathbf{S}})\mathbf{B}$ [55], where $\hat{\mathbf{S}}$ is the spin-1 matrix in SO(3) expressed as:

$$\hat{\mathbf{S}}=\left\{\hat{S}_x,\hat{S}_y,\hat{S}_z\right\}=\left\{\begin{pmatrix}0&0&0\\0&0&i\\0&-i&0\end{pmatrix},\begin{pmatrix}0&0&-i\\0&0&0\\i&0&0\end{pmatrix},\begin{pmatrix}0&i&0\\-i&0&0\\0&0&0\end{pmatrix}\right\},\tag{S16}$$

the Maxwell's equations in the form of the Dirac equation named as optical Dirac equation have been introduced and researched for years [52]

$$\hat{\mathbf{H}}\left|\Psi\right\rangle=v\begin{pmatrix}\mathbf{0}&\hat{\mathbf{S}}\\\hat{\mathbf{S}}&\mathbf{0}\end{pmatrix}\cdot\hat{\mathbf{p}}\left|\Psi\right\rangle=v\hat{\boldsymbol{\alpha}}\cdot\hat{\mathbf{p}}\left|\Psi\right\rangle=i\hbar\frac{\partial}{\partial t}\left|\Psi\right\rangle,\tag{S17}$$

with the Riemann–Silberstein (RS) vector (6-vector photon wave function) given by [53]

$$\left|\Psi\right\rangle=\frac{1}{2}\begin{pmatrix}\sqrt{\varepsilon}\mathbf{E}\\ i\sqrt{\mu}\mathbf{H}\end{pmatrix}.\tag{S18}$$

Here, $v = 1/\sqrt{\varepsilon\mu}$ is the velocity of light in medium. In the form of RS vector, the Minkowski-type canonical momentum and spin angular momentum (SAM) can be expressed as

$$\mathbf{P}^M=\frac{1}{4\omega}\mathrm{Im}\left\{\varepsilon\mathbf{E}^*\cdot(\nabla)\mathbf{E}+\mu\mathbf{H}^*\cdot(\nabla)\mathbf{H}\right\}=\frac{1}{\hbar\omega}\left\langle\Psi\right|\begin{bmatrix}\hat{\mathbf{p}}&\mathbf{0}\\\mathbf{0}&\hat{\mathbf{p}}\end{bmatrix}\left|\Psi\right\rangle=\frac{1}{\hbar\omega}\left\langle\Psi\right|\hat{\mathbf{P}}\left|\Psi\right\rangle,\tag{S19}$$

and

$$\boldsymbol{\Sigma}=\frac{1}{4\omega}\mathrm{Im}\left\{\varepsilon\mathbf{E}^*\times\mathbf{E}+\mu\mathbf{H}^*\times\mathbf{H}\right\}=\frac{1}{\hbar\omega}\left\langle\Psi\right|\hbar\begin{bmatrix}\hat{\mathbf{S}}&0\\0&\hat{\mathbf{S}}\end{bmatrix}\left|\Psi\right\rangle=\frac{1}{\hbar\omega}\left\langle\Psi\right|\hat{\boldsymbol{\Sigma}}\left|\Psi\right\rangle.\tag{S20}$$

Here, $\hat{\mathbf{p}} = -i\hbar\nabla$ is the momentum operator. Therefore, the orbital angular momentum (OAM) operator and intrinsic SAM operator are

$$\hat{\mathbf{L}}=\hat{\mathbf{r}}\times\hat{\mathbf{p}}\tag{S21}$$

and

$$\hat{\boldsymbol{\Sigma}}=\hbar\begin{bmatrix}\hat{\mathbf{S}}&0\\0&\hat{\mathbf{S}}\end{bmatrix},\tag{S22}$$

respectively.

Firstly, the time derivative of position operator $\hat{\mathbf{r}}$ can be calculated as

$$\dot{\hat{\mathbf{r}}} = \frac{i}{\hbar}\left[\hat{\mathbf{H}},\hat{\mathbf{r}}\right] = v\begin{bmatrix} 0 & \hat{\mathbf{S}} \\ \hat{\mathbf{S}} & 0 \end{bmatrix} = v\hat{\boldsymbol{\alpha}} \,. \tag{S23}$$

Thus, the underlying physics of the operator $v\hat{\boldsymbol{\alpha}}$ can be understood as the group velocity of EM field which given by the Poynting vector because there is

$$\mathbf{p}^{A} = \frac{1}{2}\mathrm{Re}\left\{\mathbf{E}^{*}\times\mathbf{H}\right\} = \frac{1}{2}\mathrm{Re}\left\{-i\left(\mathbf{E}^{*}\cdot\hat{\mathbf{S}}\right)\mathbf{H}\right\} = \left\langle\Psi\right|v\begin{bmatrix} 0 & \hat{\mathbf{S}} \\ \hat{\mathbf{S}} & 0 \end{bmatrix}\left|\Psi\right\rangle = \left\langle\Psi\right|v\hat{\boldsymbol{\alpha}}\left|\Psi\right\rangle . \tag{S24}$$

Notable that the Poynting vector $\mathbf{p}^{A}$ determines the kinetic Abraham-Poynting momentum $\mathbf{P}^{A}$ in the EM system $\mathbf{P}^{A} \propto \mathbf{p}^{A}/v^{2}$ [56].

Secondly, the conserved properties of SAM and OAM can be expressed as

$$\dot{\hat{\boldsymbol{\Sigma}}} = \frac{i}{\hbar}\left[\hat{\mathbf{H}},\hat{\boldsymbol{\Sigma}}\right] = -v\hat{\boldsymbol{\alpha}}\times\hat{\mathbf{p}} \;\text{ and }\; \dot{\hat{\mathbf{L}}} = \frac{i}{\hbar}\left[\hat{\mathbf{H}},\hat{\mathbf{L}}\right] = v\hat{\boldsymbol{\alpha}}\times\hat{\mathbf{p}} \,. \tag{S25}$$

These equations definitely show that the SAM and OAM are not conserved separately in a general EM system. However, the total angular momentum (AM) operator $\hat{\mathbf{J}} = \hat{\mathbf{L}} + \hat{\boldsymbol{\Sigma}}$ is conserved owing to

$$\dot{\hat{\mathbf{J}}} = \frac{i}{\hbar}\left[\hat{\mathbf{H}},\hat{\mathbf{J}}\right] = \frac{i}{\hbar}\left[\hat{\mathbf{H}},\hat{\mathbf{L}}\right] + \frac{i}{\hbar}\left[\hat{\mathbf{H}},\hat{\boldsymbol{\Sigma}}\right] = 0 \,. \tag{S26}$$

Obviously, the SOC is related to the operator $\hat{\mathbf{H}}_{\mathrm{SO}} = v\hat{\boldsymbol{\alpha}}\times\hat{\mathbf{p}}$. In this way, the spin-orbit interactions can be calculated as

$$\mathbf{H}_{\mathrm{SO}} = \left\langle\Psi\right|\hat{\mathbf{H}}_{\mathrm{SO}}\left|\Psi\right\rangle = \left\langle\Psi\right|v\begin{bmatrix} 0 & \hat{\mathbf{S}}\times\hat{\mathbf{p}} \\ \hat{\mathbf{S}}\times\hat{\mathbf{p}} & 0 \end{bmatrix}\left|\Psi\right\rangle = \frac{i\hbar}{4}\left[\left(\mathbf{H}^{*}\cdot\nabla\right)\mathbf{E} - \left(\mathbf{E}^{*}\cdot\nabla\right)\mathbf{H}\right]. \tag{S27}$$

Therein, the real part of $\mathbf{H}_{\mathrm{SO}}$ is

$$\mathrm{Re}\,\mathbf{H}_{\mathrm{SO}} = \mathrm{Re}\left\{\frac{i\hbar}{4}\left[\left(\mathbf{H}^{*}\cdot\nabla\right)\mathbf{E} - \left(\mathbf{E}^{*}\cdot\nabla\right)\mathbf{H}\right]\right\} = \frac{i\hbar}{4}\left[\nabla\left(\mathbf{H}^{*}\cdot\mathbf{E} - \mathbf{E}^{*}\cdot\mathbf{H}\right)\right] = -\frac{\hbar\omega}{k^{2}}\nabla C . \tag{S28}$$

This term indicates that the SOC is related to the gradient of EM helical density [56]

$$C = -\frac{\varepsilon\omega}{2}\mathrm{Im}\left\{\mathbf{E}^{*}\cdot\mathbf{B}\right\} \tag{S29}$$

in the EM system.

On the other hand, the imaginary part of $\mathbf{H}_{\mathrm{SO}}$ is

$$\mathrm{Im}\,\mathbf{H}_{\mathrm{SO}} = \mathrm{Im}\left\{\frac{i\hbar}{4}\left[\left(\mathbf{H}^{*}\cdot\nabla\right)\mathbf{E} - \left(\mathbf{E}^{*}\cdot\nabla\right)\mathbf{H}\right]\right\} = \nabla\times\frac{\hbar}{4}\mathrm{Re}\left\{\mathbf{E}\times\mathbf{H}^{*}\right\} = \frac{\hbar}{2}\nabla\times\mathbf{p}^{A} . \tag{S30}$$

This term indicates that the SOC is also related to the curl of Poynting vector/kinetic Abraham-Poynting momentum, which is proportional to the EM transverse spin

$$\mathbf{S}_{T} = \frac{1}{2\omega^{2}}\nabla\times\mathbf{p}^{A} = \frac{1}{2k^{2}}\nabla\times\mathbf{P}^{A} \tag{S31}$$

in the nondispersive medium [56]. This quantity of SOC in Eq. (S25), whose real part and imaginary part are given in Eq. (S28) and Eq. (S30), respectively, is one of key achievement in our manuscript.

To understand these SOC term, we take the paraxial Hermite-Gaussian (HG) optical beam propagating in the z-direction in Cartesian coordinates (x, y, z), in which no spin-orbit AM conversions exist approximatively, for example. However, there will still be SOCs in the system. The electric and magnetic field components can be expressed as [S2]

$$\mathbf{E}_{\mathrm{HG}} = \left[+\eta_x u_{\mathrm{HG}} \hat{\mathbf{x}}, +\eta_y u_{\mathrm{HG}} \hat{\mathbf{y}}, +\frac{1}{ik}\left(\eta_x \frac{\partial}{\partial x} + \eta_y \frac{\partial}{\partial y} \right) u_{\mathrm{HG}} \hat{\mathbf{z}} \right]^{\mathrm{T}} e^{-\mathrm{i}kz} \tag{S32}$$

and

$$\mathbf{H}_{\mathrm{HG}} = \frac{k}{\omega\mu}\left[+\eta_y u_{\mathrm{HG}} \hat{\mathbf{x}}, -\eta_x u_{\mathrm{HG}} \hat{\mathbf{y}}, +\frac{1}{ik}\left(\eta_y \frac{\partial}{\partial x} - \eta_x \frac{\partial}{\partial y} \right) u_{\mathrm{HG}} \hat{\mathbf{z}} \right]^{\mathrm{T}} e^{-\mathrm{i}kz}, \tag{S33}$$

where η_x and η_y are arbitrary complex constants describing the relative strength, $\mathrm{Im}\{\eta_x^*\eta_y\}$ specifies the polarization ellipticity (helicity) of the paraxial HG beam, and the superscript T indicates the transpose of the matrix. The complex amplitude u_{HG} is given by

$$u_{\mathrm{HG},mn} = \frac{w_0}{w(z)} H_m\left[\frac{\sqrt{2}x}{w(z)} \right] H_n\left[\frac{\sqrt{2}y}{w(z)} \right] \exp\left(-\frac{x^2+y^2}{w^2(z)} - i\frac{k\left(x^2+y^2\right)}{2R(z)} \right) \exp\left(-i\left(1+m+n\right)\tan^{-1}\left(\frac{z}{z_R} \right) \right). \tag{S34}$$

Here, $H_m(x)$ is the Hermite polynomial with non-negative integer index m, $z_R = \pi w_0^2/\lambda$ the Rayleigh range, $w(z) = w_0\sqrt{1 - z^2/z_R^2}$ the beam width of the propagating wave, w_0 the beam radius at the beam waist, $R(z)$ the radius of curvature of the wavefronts, λ the wavelength, and the last factor $\exp\left(-i(1+m+n)\tan^{-1}(z/z_R)\right)$ is the Gouy phase.

The EM helicity of paraxial HG beam and the gradient of EM helicity are

$$C_{\mathrm{HG}} = \frac{\varepsilon k}{2\mu}\mathrm{Im}\left[\eta_y^*\eta_x - \eta_y\eta_x^* \right] u_{\mathrm{HG}}^* u_{\mathrm{HG}} \tag{S35}$$

and

$$\nabla C_{\mathrm{HG}} = \frac{\varepsilon k}{2\mu}\mathrm{Im}\left[\eta_y^*\eta_x - \eta_y\eta_x^* \right] \left[\frac{\partial u_{\mathrm{HG}}^* u_{\mathrm{HG}}}{\partial x}\hat{\mathbf{x}}, \frac{\partial u_{\mathrm{HG}}^* u_{\mathrm{HG}}}{\partial y}\hat{\mathbf{y}}, 0\hat{\mathbf{z}} \right]^{\mathrm{T}}, \tag{S36}$$

respectively. Here, the z-component is ignored in the paraxial approximation ($\frac{\partial^2 u_{\mathrm{HG}}}{\partial z^2} \ll k\frac{\partial u_{\mathrm{HG}}}{\partial z} \ll k^2 u_{\mathrm{HG}}$). The horizontal components of this gradient of EM helicity are similar to the projections of the longitudinal spin component ($\mathbf{S}_L$) of paraxial HG beam into the xy-plane

$$\mathbf{S}_L = \frac{\varepsilon}{4\omega}\mathrm{Im}\left\{ \begin{array}{c} \frac{1}{ik}\left[-\left(\eta_x^*\eta_y - \eta_x\eta_y^* \right)\left(u_{\mathrm{HG}}^* \frac{\partial u_{\mathrm{HG}}}{\partial x} - u_{\mathrm{HG}} \frac{\partial u_{\mathrm{HG}}^*}{\partial x} \right) \right] \hat{\mathbf{x}} \\ \frac{1}{ik}\left[-\left(\eta_x^*\eta_y - \eta_x\eta_y^* \right)\left(u_{\mathrm{HG}}^* \frac{\partial u_{\mathrm{HG}}}{\partial y} - u_{\mathrm{HG}} \frac{\partial u_{\mathrm{HG}}^*}{\partial y} \right) \right] \hat{\mathbf{y}} \\ \left[\begin{array}{l} 2\left(\eta_x^*\eta_y - \eta_y^*\eta_x \right) u_{\mathrm{HG}}^* u_{\mathrm{HG}} \\ -\frac{1}{k^2}\left(\eta_x^*\eta_x + \eta_y^*\eta_y \right)\left(\nabla u_{\mathrm{HG}}^* \times \nabla u_{\mathrm{HG}} \right)_z + \frac{1}{2k^2}\left(\eta_x^*\eta_y - \eta_y^*\eta_x \right)\nabla_\perp^2\left(u_{\mathrm{HG}}^* u_{\mathrm{HG}} \right) \end{array} \right] \hat{\mathbf{z}} \end{array} \right\}. \tag{S37}$$

This term indicates the SOC between the longitudinal spin (EM helicity) and the intrinsic/extrinsic OAMs [43,44], which have led to the spin-orbit interaction phenomena such as spin Hall effect and spin-to-orbit AM conversions, etc. On the other hand, the imaginary part of $\mathbf{H}_{\mathrm{SO}}$ given by the vorticities of kinetic Abraham-Poynting momentum is related to the EM transverse spin

$$\mathbf{S}_T = \frac{1}{2k^2}\nabla\times\mathbf{p} = \frac{\varepsilon}{4\omega}\mathrm{Im}\left\{\begin{array}{r} \frac{1}{ik}\left[+\left(\eta_x^*\eta_x+\eta_y^*\eta_y\right)\frac{\partial u_{\mathrm{HG}}^* u_{\mathrm{HG}}}{\partial y}\right]\hat{\mathbf{x}} \\ \frac{1}{ik}\left[-\left(\eta_x\eta_x^*+\eta_y\eta_y^*\right)\frac{\partial u_{\mathrm{HG}}^* u_{\mathrm{HG}}}{\partial x}\right]\hat{\mathbf{y}} \\ \frac{1}{k^2}\left[\left(\eta_x^*\eta_x+\eta_y^*\eta_y\right)\left(\nabla u_{\mathrm{HG}}^*\times\nabla u_{\mathrm{HG}}\right)_z-\frac{1}{2}\left(\eta_x^*\eta_y-\eta_y^*\eta_x\right)\nabla_\perp^2\left(u_{\mathrm{HG}}^* u_{\mathrm{HG}}\right)\right]\hat{\mathbf{z}} \end{array}\right\}, \tag{S37}$$

in which the x- and y- components are related to the inhomogeneities/structural properties of EM field and the z-component is related to the Berry curvature of EM system [57]. This term indicates the SOC between the transverse spin and the intrinsic/extrinsic OAMs, which have led to the phenomena such as spin-momentum locking and orbit-to-spin AM conversions [23,58], etc. Notable that the total SAM is given by $\mathbf{S} = \mathbf{S}_L + \mathbf{S}_T$.

In sum, from the former analysis, the term $\mathbf{H}_{\mathrm{SO}}$ definitely describes the SOC in the EM system, and we will uncover the mechanisms of the formation of various EM spin topological defects by using this term.

III. Phenomenology of EM spin skyrmions at the multilayered systems

The phenomenological theory of the formation of specific Néel-type configuration photonic skyrmion at metal surface was performed in Ref. [29]. Here, we aim to generalize the theory to uncover the formation of various configurations of EM spin skyrmions at the multilayered system. The square modulus of total angular momentum can be expressed as

$$\mathbf{J}\cdot\mathbf{J} = \mathbf{L}\cdot\mathbf{L} + 2\mathbf{L}\cdot\mathbf{S} + \mathbf{S}\cdot\mathbf{S}. \tag{S38}$$

In the multilayered system, there is cylindrical symmetry, which is associated with the conservation of the square modulus of total AM in the normal direction (assuming in the z-direction in the cylindrical coordinates (r, φ, z)). Thus, the OAM and SAM components of Eq. (S38) are $\mathbf{L} = \mathbf{r} \times \mathbf{P}^M$ and $\mathbf{S} = \mathbf{r} \times \mathbf{P}^S$, respectively. Therein, the kinetic Abraham-Poynting momentum is decomposed into the Minkowski-type canonical momentum $\mathbf{P}^M$ and the Belinfante spin momentum $\mathbf{P}^S$, and the Belinfante spin momentum is given by $\mathbf{P}^S = \nabla \times \mathbf{\Sigma}/2$. Obviously, in physics, the variation of the integration of $\mathbf{J}\cdot\mathbf{J}$ on the local spin vector in the whole plane perpendicular to z-axis should be zero:

$$\begin{aligned}\delta\langle\mathbf{J}\cdot\mathbf{J}\rangle &= \delta\int_\infty \mathbf{J}\cdot\mathbf{J}d\Omega = \delta\int_\infty \mathbf{L}\cdot\mathbf{L}d\Omega + \delta\int_\infty 2\mathbf{L}\cdot\mathbf{S}d\Omega + \delta\int_\infty \mathbf{S}\cdot\mathbf{S}d\Omega \\ &= \delta\int_\infty \mathbf{r}\cdot\mathbf{r}P_\varphi^{M2}d\Omega + \delta\int_\infty 2\mathbf{r}\cdot\mathbf{r}P_\varphi^M P_\varphi^S d\Omega + \delta\int_\infty \mathbf{r}\cdot\mathbf{r}P_\varphi^{S2}d\Omega\end{aligned}. \tag{S39}$$

Because we only interest in the geometry of the directional vector of spin texture, we set $\mathbf{r}$ as the unit directional vector and one has $\mathbf{r}\cdot\mathbf{r}=1$, and then the Eq. (S39) can be translated into

$$\delta\langle\mathbf{J}\cdot\mathbf{J}\rangle = \delta\int_\infty \left(P_\varphi^{M2} + 2P_\varphi^M P_\varphi^S + P_\varphi^{S2}\right)d\Omega. \tag{S40}$$

Subsequently, from relativity, the Minkowski-type canonical momentum should be proportional to energy density W and decay by $1/r$-dependent for cylindrical waves (such as the surface Bessel modes [29]):

$$\mathbf{P}^{M} = \frac{\hbar\ell}{\hbar\omega}\frac{W}{r}. \tag{S41}$$

Here, ℓ is the quantum number of OAM. By carefully choosing the relative complex amplitude of electric/magnetic fields, we can obtain $W = \hbar\omega$ for a single wave packet. Therefore, the OAM term is a constant quantity and the variation of OAM term on the local spin vector is zero: $\delta\mathbf{L} = 0$. Then, as the situation of magnetic skyrmions [6], one can assume that the normalized local spin vector $\mathbf{\Sigma}$ has an expression of

$$\mathbf{\Sigma} = \hbar\sigma_h\left[\sin\Theta\cos\Phi\hat{\mathbf{r}}, \sin\Theta\sin\Phi\hat{\boldsymbol{\varphi}}, \cos\Theta\hat{\mathbf{z}}\right] \tag{S42}$$

by ignoring the dependent of Θ and Φ on z-axis and considering $\Theta = \Theta(r,\varphi)$ and $\Phi = \Phi(r,\varphi)$ for the spin vector of a single wave packet. In particular, for the Néel-type, Bloch-type and twisted type skyrmions discussed in our manuscript, we can further set that $\Theta = \Theta(r)$ and Φ = Constant. Then, the variational equation Eq. (S40) can be calculated as

$$\delta\langle\mathbf{J}\cdot\mathbf{J}\rangle = \frac{\hbar^2\sigma^2}{4}\int_0^\infty \delta\Theta\left\{\begin{array}{l} -2\left(\sin^2\Theta + \cos^2\Theta\sin^2\Phi\right)\dfrac{\partial^2\Theta}{\partial r^2} \\ -\sin 2\Theta\left(\sin\Phi + \cos 2\Phi\right)\left(\dfrac{\partial\Theta}{\partial r}\right)^2 + \dfrac{2\sin 2\Theta\sin^2\Phi}{r^2} \end{array}\right\}dr, \tag{S43}$$

where we use the calculus

$$\begin{aligned} &\int_0^\infty\left[2\left(\sin^2\Theta + \cos^2\Theta\sin^2\Phi\right)\frac{\partial\Theta}{\partial r} + \frac{\sin 2\Theta\sin^2\Phi}{r}\right]\delta\left(\frac{\partial\Theta}{\partial r}\right)dr \\ &= \int_0^\infty \delta\Theta\left[\frac{\sin 2\Theta\sin^2\Phi}{r^2} - \frac{2\cos 2\Theta\sin^2\Phi}{r}\frac{\partial\Theta}{\partial r} - 2\sin 2\Theta\cos^2\Phi\left(\frac{\partial\Theta}{\partial r}\right)^2 - 2\left(\sin^2\Theta + \cos^2\Theta\sin^2\Phi\right)\frac{\partial^2\Theta}{\partial r^2}\right]dr \end{aligned}. \tag{S44}$$

For the **Néel-type skyrmion**, there is $\Phi = 0$, and the variational equation is downgraded to

$$-2\sin^2\Theta\frac{\partial^2\Theta}{\partial r^2} - \sin 2\Theta\left(\frac{\partial\Theta}{\partial r}\right)^2 = 0. \tag{S45}$$

The nontrivial solution of this partial differential equation (S45) is

$$\Theta(r) = \pm\arccos\left[-c_1 r - c_1 c_2\right], \tag{S46}$$

The constants c_1 and c_2 are determined by the boundary conditions.

For the **Bloch-type skyrmion**, there is $\Phi = \pi/2$, and the variational equation is downgraded to

$$-2\frac{\partial^2\Theta}{\partial r^2} + \frac{2\sin 2\Theta}{r^2} = 0. \tag{S47}$$

By specifying $r = e^t$, the equation is translated to

$$\frac{\partial^2\Theta}{\partial t^2} - \frac{\partial\Theta}{\partial t} - \sin 2\Theta = 0. \tag{S48}$$

For the **twisted skyrmion**, we can specify that $\Phi = \pi/4$, and the variational equation is downgraded to

$$-\left(1 + \sin^2\Theta\right)\frac{\partial^2\Theta}{\partial r^2} - \frac{\sqrt{2}}{2}\sin 2\Theta\left(\frac{\partial\Theta}{\partial r}\right)^2 + \frac{\sin 2\Theta}{r^2} = 0. \tag{S49}$$

By specifying $r = e^t$, the equation is translated to

$$\frac{\partial^2\Theta}{\partial t^2}+\frac{\sqrt{2}}{2}\frac{\sin 2\Theta}{1+\sin^2\Theta}\left(\frac{\partial\Theta}{\partial t}\right)^2-\frac{\partial\Theta}{\partial t}-\frac{\sin 2\Theta}{1+\sin^2\Theta}=0\,. \tag{S50}$$

The Eq. (S48) and Eq. (S50) can be solved numerically. By solving these partial differential equations by MATHEMATICA, one can obtain the similar curves as that shown in Fig. S1, which indicates the spin vector varies from centre 'up' state to boundary 'down' state gradually without discontinuities/singularities. The skyrmion number of these spin textures

$$N_{\mathrm{SK}}=\frac{1}{4\pi}\iint_{\Omega}\mathbf{M}\cdot\left(\frac{\partial\mathbf{M}}{\partial x}\times\frac{\partial\mathbf{M}}{\partial y}\right)dxdy \tag{S51}$$

with the normalized spin vector $\mathbf{M}=\mathbf{\Sigma}/|\mathbf{\Sigma}|$ is equal to -1 universally and the configurations of EM spin skyrmions can be tuned by the SOCs.

In the section V, we will investigate the SOCs of various EM modes akin to those in magnetic skyrmions to analyze the transitions between the various configurations of EM topological textures.

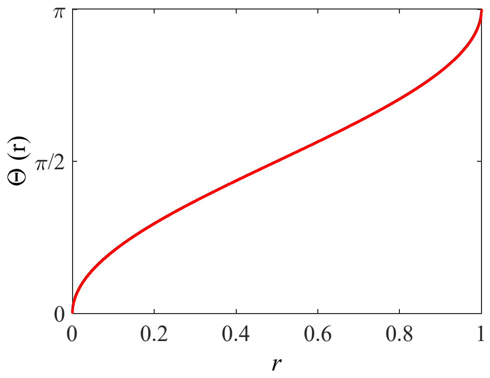

Fig. S1. The solution of partial differential equation (S45). The boundary conditions include $\Theta(0)=0$ and $\Theta(1)=\pi$. For the Eq. (S48) and Eq. (S50), the abscissa axis is t.

IV. Various EM modes and EM field topological structures

1. Electric field topological quasiparticles in surface plasmon polariton modes

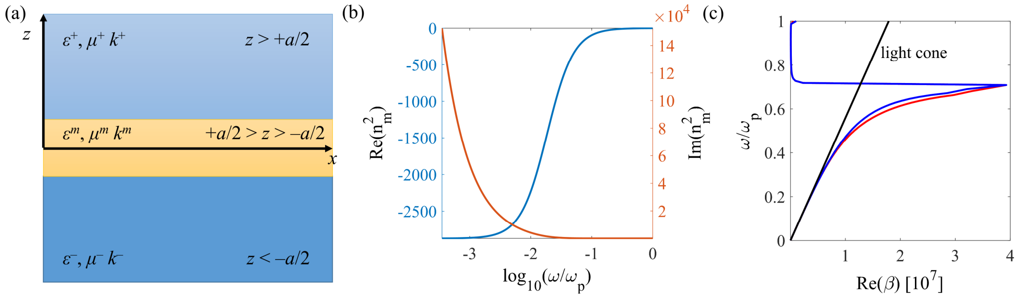

Fig. S2. (a) Schematic diagram of one-layer configuration containing lossy metal to excite the *p*-polarized surface modes (surface plasmons polaritons: SPPs). The interfaces are localized between the planes $z=+a/2$ and $z=-a/2$. (b) The permittivity of metal film and (c) the angular frequency (ω/ω_p) via the propagating constant Re(β). $\omega_p\approx 5.36\times10^{15}/s$ ($\lambda_p\approx 0.35\times10^{-6}m$) is the plasma frequency and the characteristic frequency $\gamma=10^{14}/s$. The red/blue lines denote the symmetric/anti-symmetric surface modes of air-metal-air structure with the thickness equal to 0.2λ. The black line represents the light cone of vacuum. $k_0=\omega/c$ is the wavenumber in vacuum.

Multilayered configuration is beneficial for designing and fabricating the dispersion-engineered artificial metamaterials [47,48]. For the lossy metal in the multilayered systems (**Fig. S2(a)**), the permittivity $\varepsilon(\omega)$ (refractive index $n(\omega)$) is

$$\varepsilon(\omega)=\varepsilon_0 n^2(\omega)=\varepsilon_0\left(1-\frac{\omega_p^2}{\omega^2+i\omega\gamma}\right)=\varepsilon_0\left(1-\frac{\omega_p^2}{\omega^2+\gamma^2}+i\frac{\omega_p^2}{\omega^3/\gamma+\omega\gamma}\right). \tag{S52}$$

For the noble metal, it is naturally that the characteristic frequency $\gamma \approx 10^{14}\mathrm{H_z}$ and $\omega_p \approx 10^{16}\mathrm{H_z}$. Thus, we use the characteristic frequency $\gamma \approx 10^{14}\mathrm{H_z}$ and consider $\omega < \omega_p$. Thus, the real part of permittivity is negative: $\mathrm{Re}\{\varepsilon(\omega)\} < 0$ (**Fig. S2(b)**).

For the insulator-metal-insulator system shown in **Fig. S2(a)**, only the p-polarized (transverse magnetic, TM) surface EM mode can be excited [S3]. The electric/magnetic field components of the p-polarized surface modes in Cartesian coordinates (x, y, z) are summarized in **Table S1**:

Table S1. Electric/Magnetic field components of the p-polarized surface EM modes

Region	$z>+\frac{a}{2}$	$-\frac{a}{2}<z<+\frac{a}{2}$	$z<-\frac{a}{2}$
Electric field	$E_x^+=-\frac{k_z^+}{\beta^2}\frac{\partial E_z^+}{\partial x}$	$E_x^m=E_x^{m+}+E_x^{m-}=+\frac{k_z^m}{\beta^2}\frac{\partial E_z^{m+}}{\partial x}-\frac{k_z^m}{\beta^2}\frac{\partial E_z^{m-}}{\partial x}$	$E_x^-=+\frac{k_z^-}{\beta^2}\frac{\partial E_z^-}{\partial x}$
	$E_y^+=-\frac{k_z^+}{\beta^2}\frac{\partial E_z^+}{\partial y}$	$E_y^m=E_y^{m+}+E_y^{m-}=+\frac{k_z^m}{\beta^2}\frac{\partial E_z^{m+}}{\partial y}-\frac{k_z^m}{\beta^2}\frac{\partial E_z^{m-}}{\partial y}$	$E_y^-=+\frac{k_z^-}{\beta^2}\frac{\partial E_z^-}{\partial y}$
	$E_z^+=\frac{A_+}{\varepsilon^+}\xi e^{-k_z^+(z-a/2)}$	$E_z^m=E_z^{m+}+E_z^{m-}=\frac{B_+}{\varepsilon^m}\xi e^{+k_z^m(z-a/2)}+\frac{B_-}{\varepsilon^m}\xi e^{-k_z^m(z+a/2)}$	$E_z^-=\frac{A_-}{\varepsilon^-}\xi e^{+k_z^-(z+a/2)}$
Magnetic field	$H_x^+=-\frac{i\omega\varepsilon^+}{\beta^2}\frac{\partial E_z^+}{\partial y}$	$H_x^m=H_x^{m+}+H_x^{m-}=-\frac{i\omega\varepsilon^m}{\beta^2}\frac{\partial E_z^{m+}}{\partial y}-\frac{i\omega\varepsilon^m}{\beta^2}\frac{\partial E_z^{m-}}{\partial y}$	$H_x^-=-\frac{i\omega\varepsilon^-}{\beta^2}\frac{\partial E_z^-}{\partial y}$
	$H_y^+=+\frac{i\omega\varepsilon^+}{\beta^2}\frac{\partial E_z^+}{\partial x}$	$H_y^m=H_y^{m+}+H_y^{m-}=+\frac{i\omega\varepsilon^m}{\beta^2}\frac{\partial E_z^{m+}}{\partial x}+\frac{i\omega\varepsilon^m}{\beta^2}\frac{\partial E_z^{m-}}{\partial x}$	$H_y^-=+\frac{i\omega\varepsilon^-}{\beta^2}\frac{\partial E_z^-}{\partial x}$
	$H_z^+=0$	$H_z^m=0$	$H_z^-=0$

Here, $i = +, -$ and m are corresponding to the regions $z > +a/2$, $z < -a/2$ and $-a/2 < z < +a/2$, respectively. $\xi(x,y)$ is the function of horizontal coordinates (x,y) and satisfies the transverse Helmholtz equation $\nabla_\perp^2\xi+\beta^2\xi=0$ with $\nabla_\perp^2=\partial^2/\partial x^2+\partial^2/\partial y^2$. By considering the EM boundary conditions, the dispersion relation can be expressed as [S3]

$$e^{-2k_z^m a}=\frac{\left(k_z^m/\varepsilon^m+k_z^+/\varepsilon^+\right)\left(k_z^m/\varepsilon^m+k_z^-/\varepsilon^-\right)}{\left(k_z^m/\varepsilon^m-k_z^+/\varepsilon^+\right)\left(k_z^m/\varepsilon^m-k_z^-/\varepsilon^-\right)}. \tag{S53}$$

Here, the propagating constant (horizontal wavevector) β is expressed as

$$\beta^2=k^i(\omega)\cdot k^i(\omega)+k_z^i\cdot k_z^i=\omega^2\varepsilon^i(\omega)\mu^i+k_z^i\cdot k_z^i, \tag{S54}$$

where k^i is the total wavenumber and k_z^i is z-component wavenumber of i-th layer. Here, it is worth noting that the propagating constant β is a complex number for the lossy mode [61], where the real part indicates the propagating property and the imaginary part represents the attenuation. The field parameters are

$$\frac{B_+}{B_-} = \frac{k_z^m/\varepsilon^m - k_z^+/\varepsilon^+}{k_z^m/\varepsilon^m + k_z^+/\varepsilon^+} e^{-k_z^m a} \quad \frac{B_-}{B_+} = \frac{k_z^m/\varepsilon^m - k_z^-/\varepsilon^-}{k_z^m/\varepsilon^m + k_z^-/\varepsilon^-} e^{-k_z^m a} \quad \begin{matrix} +A_+ = +B_+ + B_- e^{-k_z^m a} \\ +B_+ e^{-k_z^m a} + B_- = +A_- \end{matrix} . \tag{S55}$$

Since only the relative amplitude makes physical sense, one can set one of A_+, B_+, B_- and A_- to be 1 and the other amplitude coefficients can be calculated properly.

Particularly, for the air-metal-air structure considered in our manuscript, there is $\varepsilon^+ = \varepsilon^- = \varepsilon_0$. Here, ε_0 is the permittivity of air. Therefore, the dispersion relation (S53) can be re-expressed as

$$+e^{-k_z^m a} = \frac{k_z^m/\varepsilon^m + k_z^+/\varepsilon_0}{k_z^m/\varepsilon^m - k_z^+/\varepsilon_0} \tag{S56}$$

for the symmetric modes and

$$-e^{-k_z^m a} = \frac{k_z^m/\varepsilon^m + k_z^+/\varepsilon_0}{k_z^m/\varepsilon^m - k_z^+/\varepsilon_0} \tag{S57}$$

for the anti-symmetric mode. The dispersion relations of the symmetric and antisymmetric modes are shown in the red and blue lines of **Fig. S2(c)**, respectively. If the thickness of layer is thick enough, the left terms of both Eq. (S56) and Eq. (S57) are zero approximatively, and hence the propagation constants can be expressed universally as

$$\beta = \omega\sqrt{\frac{\varepsilon^m \varepsilon_0}{\varepsilon_0 + \varepsilon^m}\mu_0} = \frac{\omega}{c}\sqrt{\frac{\varepsilon^m/\varepsilon_0}{1+\varepsilon^m/\varepsilon_0}} . \tag{S58}$$

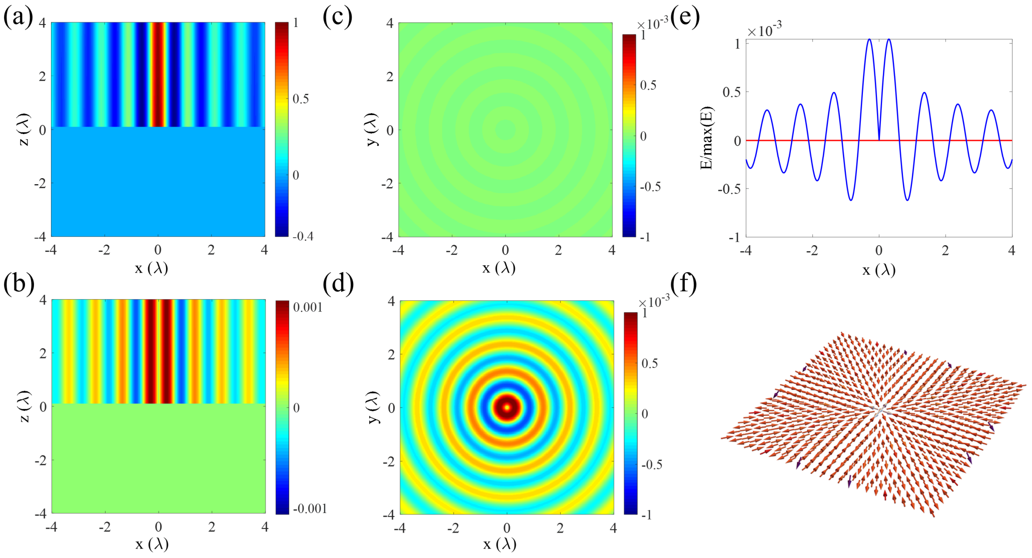

Fig. S3. Electric field defect constructed by the 0-order Bessel surface mode at a low frequency limit. The real parts of (a) *z*- and (b) radial electric field components in *xz*-plane ($y = 0$). In the metal layer, the real parts of (c) *z*- and (d) radial electric field components in *xy*-plane ($z = a/2 - 10\text{nm}$), and the corresponding (e) 1D contour at $y = 0$ and (f) electric field texture (region: $8\lambda\times 8\lambda$). One can find that the amplitude of radial component electric field is much larger that of *z*-component electric field, which makes that the skyrmion number of electric field texture is approximatively zero ($N_{SK} = 0$). Here, the wavelength $\lambda = 1\times 10^{-3} m$. The angular frequency $\omega = 1.88\times 10^{12}/s$. a is the thickness of metal and here we set $a = 0.2\lambda$.

In the following, we analyze the electric field topological defects in the multilayered air-metal-air structure. We primarily take the 0-order Bessel-type surface mode, which was known as electric field skyrmions in various references [18,20], for instance. We must emphasize that the results can be generalized into other electric field topological defects because these topological defects can be constructed with the superposition of Bessel-type mode arranged in a specific symmetry [26].

If the frequency is small enough (such as terahertz wave with $\omega << \omega_p$), one can find that $1 + \varepsilon^m/\varepsilon_0 \approx \varepsilon^m/\varepsilon_0$ and the propagating constant $\beta \approx k^{\pm} = k_0$ is a pure real number approximatively. In the case, the decaying factors in the upper/lower subspace are $k_z^{\pm} = \sqrt{\beta^2 - (k^{\pm})^2} \approx 0$. The horizontal electric field components are zero approximatively (**Fig. S3(a-b)**), especially at a low frequency limit, and thus the topological defects constructed by the electric field of 0-order Bessel-type surface mode are considered as a combination of purely 'up' state and 'down' state. While in the metal layer, there is $k_z^m = \sqrt{\beta^2 - (k^m)^2} \gg \beta$. The horizontal electric field components are much larger than the normal electric field component (**Fig. S3(c-d)**). At a low frequency limit, the normal electric field component can be ignored and thus the skyrmion number of the topological defects constructed by the electric field of 0-order Bessel-type surface mode can be considered as zero ($N_{SK} = 0$) (**Fig. S3(e-f)**). In addition, the electric field skyrmion lattice constructed by this SPP mode in C6 symmetry can be found in **Fig. 3(a)** in main text, whose skyrmion number is also considered as zero ($N_{SK} = 0$).

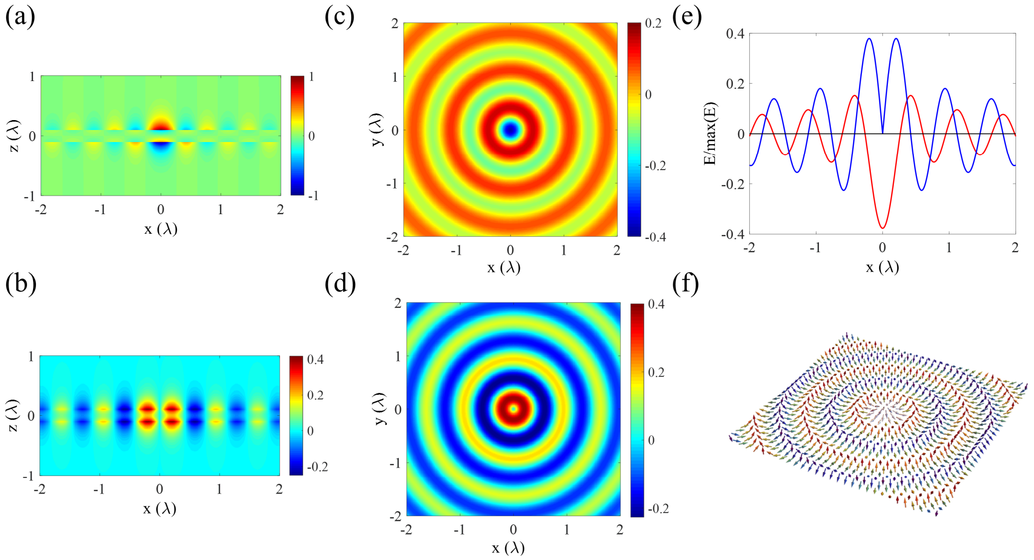

Fig. S4. Electric field defect constructed by the 0-order Bessel-type surface mode at visible frequency. The real parts of (a) z- and (b) radial electric field components in xz-plane ($y = 0$). In the metal layer, the real parts of (c) z- and (d) radial electric field components in xy-plane ($z = a/2$ – 10nm), and the corresponding (e) 1D contour at $y = 0$ and (f) electric field texture (region: $3\lambda\times3\lambda$). For the electric field texture in the upper/lower subspace or in the metal layer, one can also find that the electric field vector whirls from 'down' state to 'up' state along the radial direction, which is a manifestation Néel-type topological texture. Here, $\lambda = 6.38\times10^{-7}m$, which is corresponding to the angular frequency $\omega = 2.95\times10^{15}/s$. a is the thickness of metal and here we set $a = 0.2\lambda$.

As the frequency increases (for example, in the near-infrared or visible region), the propagating constant is a complex number and $\mathrm{Re}(\beta) > k_0$ owing to the fact that $\mathrm{Re}(\varepsilon^m/\varepsilon_0) < \mathrm{Re}(1+\varepsilon^m/\varepsilon_0) < 0$. In the instance, the z-component wavenumber $k_z^m = \sqrt{\beta^2 - (k^m)^2}$ has a same order of magnitudes with the propagating constant β. The azimuthal electric field component is always zero for the p-polarized 0-order Bessel-type surface mode and the electric field vector varies from the 'down' state to 'up' state in the radial direction (Néel-type) (**Fig. S4**). Therefore, the electric field vector of field skyrmion lattice constructed by this lossy SPP mode in C6 symmetry (**Fig. 3(b)** in main text) whirls along the radial direction and its skyrmion number is +1 ($N_{SK} = +1$) in the metal layer. Noteworthily, owing to the boundary condition from Maxwell's equations, the normal electric field components are inverted and the horizontal electric field components are continuous through the interface.

At the lossless limit, the topological properties of electric field topological defects are similar to those of lossy metal (**Fig. S5**), which indicates that the lossy property of material does not affect the topological geometries of these electric field topological defects. Thus, the skyrmion number of the electric field skyrmion lattice constructed by this lossless SPP mode in C6 symmetry is also +1 (**Fig. 3(b)** in main text).

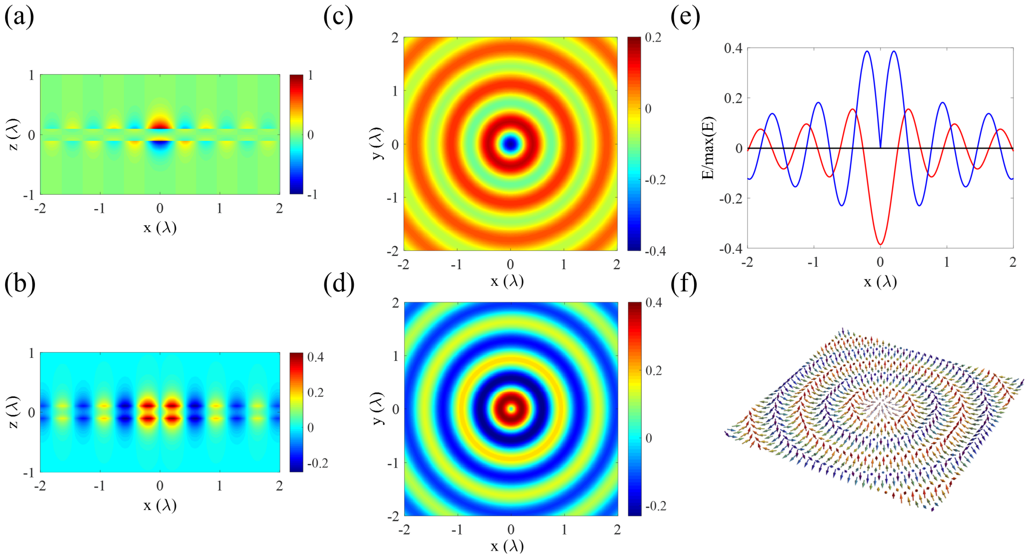

Fig. S5. Electric field defect constructed by the 0-order Bessel-type surface mode at the lossless limit. The real parts of (a) *z*- and (b) radial electric field components in *xz*-plane ($y = 0$). In metal layer, the real parts of (c) *z*- and (d) radial electric field components in *xy*-plane ($z = a/2 - 10$nm), and the corresponding (e) 1D contour at $y = 0$ and (f) electric field texture (region: 3λ×3λ). One can also find that the electric field vector whirls from 'down' state to 'up' state along the radial direction, which is a manifestation Néel-type topological texture. Here, $\gamma = 0$, $\lambda = 6.38\times10^{-7} m$, which is corresponding to the angular frequency $\omega = 2.95\times10^{15}/s$. a is the thickness of metal and here we set $a = 0.2\lambda$.

Furthermore, as the frequency increases further and approaches the plasma frequency ω_p ($\omega_p/\sqrt{2} < \omega < \omega_p$), the imaginary part of permittivity can be ignored and there will be $1 + \varepsilon^m/\varepsilon_0 > 0$ and $\varepsilon^m/\varepsilon_0 < 0$. In the case, the propagating constant β is a pure imaginary number and the propagating mode is forbidden, which was known as band gap as indicated by part **IV** in **Fig. 1(a)**.

2. Electric field topological quasiparticles in slot waveguide modes

If the frequency is larger than the plasma frequency $\omega > \omega_p$, the loss can be ignored and the permittivity is

$$0 < \varepsilon(\omega) = \varepsilon_0\left(1 - \frac{\omega_p^2}{\omega^2}\right) < \varepsilon_0 . \tag{S59}$$

The relative permittivity can be found in **Fig. S6(a)**.

In the case, the slot-waveguide-like modes (contain symmetric TE and TM modes) will be excited in the aire-medium-air structure. We must emphasize that, to produce the slot-waveguide-like modes, there should be another two interfaces as shown in Ref. [62]. Here, we assume the two interfaces localized at infinity. Although this will make the total energy density in air infinite, it would not affect the field distributions in the layer or near the air/medium interfaces. The electric/magnetic field components of the slot-waveguide-like modes in Cartesian coordinates (x, y, z) are summarized in **Table S2**.

Table S2. Electric/Magnetic field components of the **slot-waveguide-like** modes

	$z>+\frac{a}{2}$	$-\frac{a}{2}<z<+\frac{a}{2}$	$z<-\frac{a}{2}$
E_x	$+C^{E+}\left(-\frac{W^E}{\beta^{E2}}\right)\frac{\partial\xi^E}{\partial x}\sin\left(W^E z\right)$ $+C^{H+}\frac{i\omega\mu^+}{\beta^{H2}}\frac{\partial\xi^H}{\partial y}\cos\left(W^H z\right)$	$+A^{Em}\left(+\frac{U^E}{\beta^{E2}}\right)\frac{\partial\xi^E}{\partial x}e^{+U^E z}+A^{Hm}\frac{i\omega\mu^m}{\beta^{H2}}\frac{\partial\xi^H}{\partial y}e^{+U^H z}$ $+B^{Em}\left(-\frac{U^E}{\beta^{E2}}\right)\frac{\partial\xi^E}{\partial x}e^{-U^E z}+B^{Hm}\frac{i\omega\mu^m}{\beta^{H2}}\frac{\partial\xi^H}{\partial y}e^{-U^H z}$	$+D^{E-}\left(-\frac{W^E}{\beta^{E2}}\right)\frac{\partial\xi^E}{\partial r}\sin\left(W^E z\right)$ $+D^{H-}\frac{i\omega\mu^-}{\beta^{H2}}\frac{\partial\xi^H}{\partial y}\cos\left(W^H z\right)$
E_y	$+C^{E+}\left(-\frac{W^E}{\beta^{E2}}\right)\frac{\partial\xi^E}{\partial y}\sin\left(W^E z\right)$ $-C^{H+}\frac{i\omega\mu^+}{\beta^{H2}}\frac{\partial\xi^H}{\partial x}\cos\left(W^H z\right)$	$+A^{Em}\left(+\frac{U^E}{\beta^{E2}}\right)\frac{\partial\xi^E}{\partial y}e^{+U^E z}-A^{Hm}\frac{i\omega\mu^m}{\beta^{H2}}\frac{\partial\xi^H}{\partial x}e^{+U^H z}$ $+B^{Em}\left(-\frac{U^E}{\beta^{E2}}\right)\frac{\partial\xi^E}{\partial y}e^{-U^E z}-B^{Hm}\frac{i\omega\mu^m}{\beta^{H2}}\frac{\partial\xi^H}{\partial x}e^{-U^H z}$	$+D^{E-}\left(-\frac{W^E}{\beta^{E2}}\right)\frac{\partial\xi^E}{\partial y}\sin\left(W^E z\right)$ $-D^{H-}\frac{i\omega\mu^-}{\beta^{H2}}\frac{\partial\xi^H}{\partial x}\cos\left(W^H z\right)$
E_z	$C^{E+}\xi^E\cos\left(W^E z\right)$	$A^{Em}\xi^E e^{+U^E z}+B^{Em}\xi^E e^{-U^E z}$	$D^{E-}\xi^E\cos\left(W^E z\right)$
H_x	$-C^{E+}\frac{i\omega\varepsilon^+}{\beta^{E2}}\frac{\partial\xi^E}{\partial y}\cos\left(W^E z\right)$ $+C^{H+}\left(-\frac{W^H}{\beta^{H2}}\right)\frac{\partial\xi^H}{\partial x}\sin\left(W^H z\right)$	$-A^{Em}\frac{i\omega\varepsilon^m}{\beta^{E2}}\frac{\partial\xi^E}{\partial y}e^{+U^E z}+A^{Hm}\left(+\frac{U^H}{\beta^{H2}}\right)\frac{\partial\xi^H}{\partial x}e^{+U^H z}$ $-B^{Em}\frac{i\omega\varepsilon^m}{\beta^{E2}}\frac{\partial\xi^E}{\partial y}e^{-U^E z}+B^{Hm}\left(-\frac{U^H}{\beta^{H2}}\right)\frac{\partial\xi^H}{\partial x}e^{-U^H z}$	$-D^{E-}\frac{i\omega\varepsilon^-}{\beta^{E2}}\frac{\partial\xi^E}{\partial y}\cos\left(W^E z\right)$ $+D^{H-}\left(-\frac{W^H}{\beta^{H2}}\right)\frac{\partial\xi^H}{\partial x}\sin\left(W^H z\right)$
H_y	$+C^{E+}\frac{i\omega\varepsilon^+}{\beta^{E2}}\frac{\partial\xi^E}{\partial x}\cos\left(W^E z\right)$ $+C^{H+}\left(-\frac{W^H}{\beta^{H2}}\right)\frac{\partial\xi^H}{\partial y}\sin\left(W^H z\right)$	$+A^{Em}\frac{i\omega\varepsilon^m}{\beta^{E2}}\frac{\partial\xi^E}{\partial x}e^{+U^E z}+A^{Hm}\left(+\frac{U^H}{\beta^{H2}}\right)\frac{\partial\xi^H}{\partial y}e^{+U^H z}$ $+B^{Em}\frac{i\omega\varepsilon^m}{\beta^{E2}}\frac{\partial\xi^E}{\partial x}e^{-U^E z}+B^{Hm}\left(-\frac{U^H}{\beta^{H2}}\right)\frac{\partial\xi^H}{\partial y}e^{-U^H z}$	$+D^{E-}\frac{i\omega\varepsilon^-}{\beta^{E2}}\frac{\partial\xi^E}{\partial x}\cos\left(W^E z\right)$ $+D^{H-}\left(-\frac{W^H}{\beta^{H2}}\right)\frac{\partial\xi^H}{\partial y}\sin\left(W^H z\right)$
H_z	$C^{H+}\xi^H\cos\left(W^H z\right)$	$A^{Hm}\xi^H e^{+U^H z}+B^{Hm}\xi^H e^{-U^H z}$	$D^{H-}\xi^H\cos\left(W^H z\right)$

Therein, the electric and magnetic Hertz potentials fulfil the transverse Helmholtz equations:

$$\nabla_\perp^2\xi^E+\beta^{E2}\xi^E=0\quad\nabla_\perp^2\xi^H+\beta^{H2}\xi^H=0$$

in the layer and the surround materials. The superscript E and H represent the electric modes (TM modes) and magnetic (transverse electric: TE modes) modes, respectively. By considering the boundary conditions, the dispersion relation can be expressed as

$$\frac{\varepsilon^m}{U^E}\coth\left(\frac{U^E a}{2}\right)=-\frac{\varepsilon^\pm}{W^E}\cot\left(\frac{W^E a}{2}\right)\tag{S60}$$

for the electric mode, and

$$\frac{\mu^m}{U^H}\coth\left(\frac{U^H a}{2}\right)=-\frac{\mu^\pm}{W^H}\cot\left(\frac{W^H a}{2}\right)\tag{S61}$$

for the magnetic mode. Here, the parameters U^E, W^E, U^H and W^H can be calculated by

$$\begin{array}{ll} W^{E2}=k^{\pm2}-\beta^{E2} & W^{H2}=k^{\pm2}-\beta^{H2} \\ U^{E2}=\beta^{E2}-k^{m2} & U^{H2}=\beta^{H2}-k^{m2} \end{array}.\tag{S62}$$

By solving the propagation constants β^E and β^H (pure real numbers), the field parameters are

$$\begin{array}{llll} A^{Em}=B^{Em} & C^{E+}=D^{E-} & A^{Em}=C^{E+}\dfrac{\varepsilon^{+}}{\varepsilon^{m}}\cos\left(+\dfrac{W^{E}a}{2}\right)\Big/\left[\exp\left(+\dfrac{U^{E}a}{2}\right)+\exp\left(-\dfrac{U^{E}a}{2}\right)\right] \\ A^{Hm}=B^{Hm} & C^{H+}=D^{H-} & A^{Hm}=C^{H+}\dfrac{\mu^{+}}{\mu^{m}}\cos\left(+\dfrac{W^{H}a}{2}\right)\Big/\left[\exp\left(+\dfrac{U^{H}a}{2}\right)+\exp\left(-\dfrac{U^{H}a}{2}\right)\right] \end{array}. \tag{S63}$$

Since only the relative amplitude makes physical sense, one can set A^{Hm} to be 1 and $A^{Em}=\pm i\sqrt{\mu_0/\varepsilon_0}$, and then the field distributions excited by circularly polarized light can be calculated properly. The dispersion relations of the symmetric TM and TE modes are shown in the red and blue lines of **Fig. S6(b-c)**, respectively.

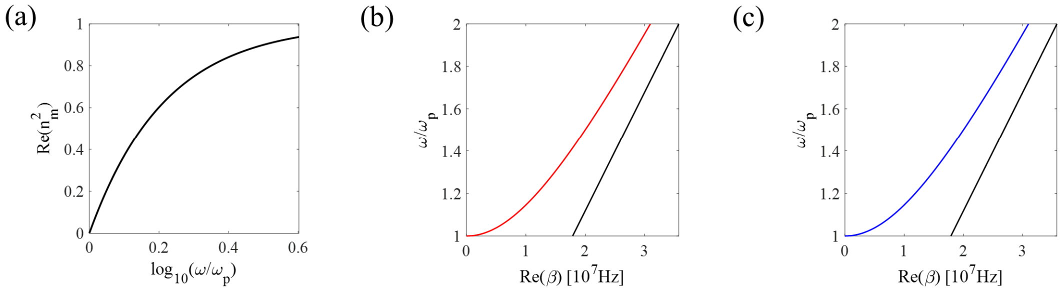

Fig. S6. Relative permittivity and dispersive relations of slot-waveguide-like modes at air-medium-air structure. (a) the relative permittivity of medium via the frequency in the situation $\omega > \omega_p$; the propagating constants of (b) symmetric electric modes and (c) symmetric magnetic modes via the frequency. Since the slot-waveguide-like mode is occupied in the whole space, the propagating constants of these symmetric electric and magnetic modes are equal. The black lines represent the light cones in air. The thickness of layer is equal to 0.2λ. $\omega_p \approx 5.36\times10^{15}/s$ ($\lambda_p \approx 0.35\times10^{-6}m$) is the plasma frequency and the characteristic frequency $\gamma = 10^{14}/s$.

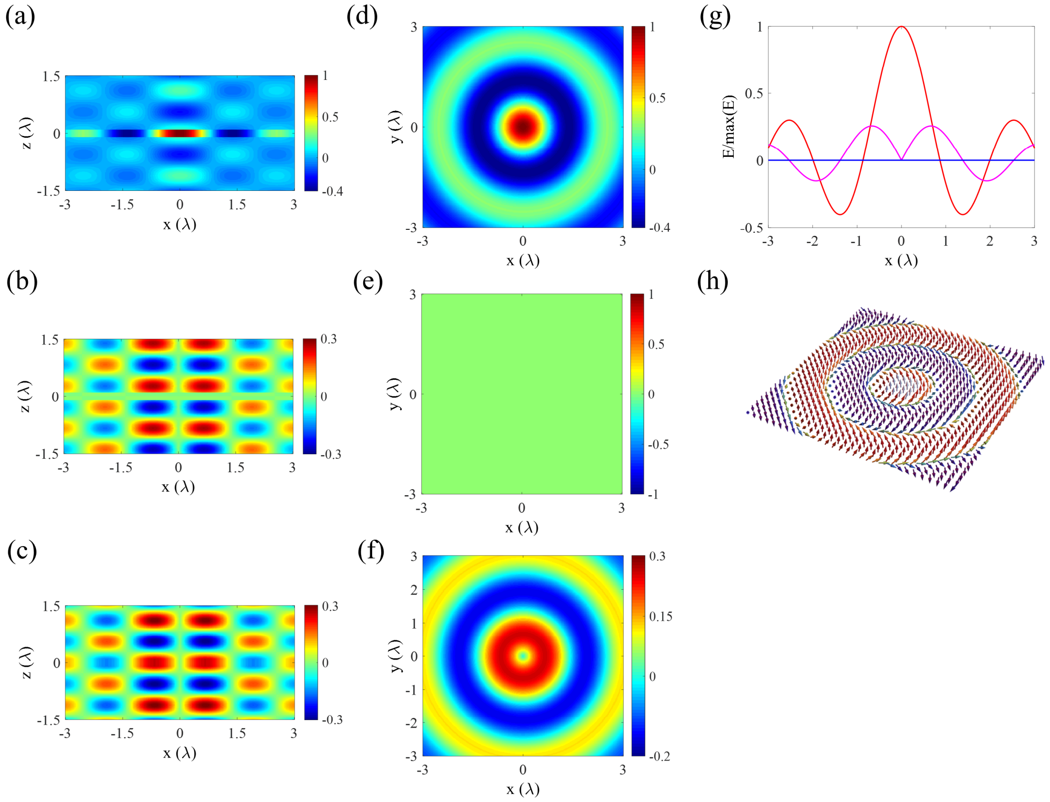

Fig. S7. Electric field defect constructed by the 0-order Bessel-type surface mode for $\omega > \omega_p$. The imaginary parts of (a) z-, (b) radial and (c) azimuthal electric field components in xz-plane (y = 0). In the layer, the imaginary parts of (d) z-, (e) radial and (f) azimuthal electric field components in *xy*-plane ($z = 0$), and the corresponding (g) 1D contour at $y = 0$ and (m) electric field texture (region: $8\lambda\times8\lambda$). It is worth noting that one can transform the imaginary part into the real part by add an additional constant phase to the amplitude. It can be found that, in the medium layer, the electric field vector whirls from 'up' state to 'down' state along the azimuthal direction, which is a manifestation of Bloch-type topological texture. Here, $\lambda = 3.33\times10^{-7}m$, which is corresponding to the angular frequency $\omega = 5.66\times10^{15}/s$. a is the thickness of metal and here we set $a = 0.2\lambda$.

In the case, since the slot-waveguide-like mode is occupied in the whole space, the propagating constants of symmetric electric and magnetic modes are equal approximatively. In air, the azimuthal and radial electric field components exist simultaneously for the 0-order Bessel-type surface mode (**Fig. S7(a-c)**). The electric field vector varies from the 'up/down' state to 'down/up' state along the radial and azimuthal directions simultaneously, and thus the electric field textures can be considered as twisted configurations in the upper/lower subspace. While in the medium layer, the radial electric field component cancels out due to the mode's coupling (**Fig. S7(b,e)**). Thus, the electric field topological defect in the layer can be considered as Bloch-type configuration (**Fig. S7(g-h)**). And the skyrmion number of this electric field skyrmion lattice constructed by this slot-waveguide-like mode in C6 symmetry is −1 (**Fig. 3(c)**). Noteworthily, owing to the boundary condition from Maxwell's equations, the normal electric field components are parallel and the horizontal electric field components are continuous through the interface (**Fig. S7**).

3. Electric field topological quasiparticles in dielectric waveguide wave mode

For the dielectrics, the damping can be ignored naturally the permittivity is (**Fig. S8(a)**)

$$\varepsilon(\omega) = \varepsilon_0\left(1+\sum_i \frac{f_i\omega_p^2}{\omega_i^2-\omega^2}\right). \tag{S64}$$

The relative permittivity can be found in **Fig. S8(a)**.

In the case, the waveguide modes (contain symmetric and anti-symmetric TE and TM modes) will be produced in the dielectric layer. The electric/magnetic field components of the waveguide modes in Cartesian coordinates (x, y, z) are summarized in **Table S3**.

Therein, the electric and magnetic Hertz potentials fulfil the transverse Helmholtz equations:

$$\nabla_\perp^2\xi^E + \beta^{E2}\xi^E = 0 \quad \nabla_\perp^2\xi^H + \beta^{H2}\xi^H = 0 \tag{S65}$$

in the metal region and surround materials. The superscripts E and H represent the electric modes and magnetic modes, respectively. By considering the boundary conditions, the dispersion relations can be expressed as

$$\frac{\varepsilon^m}{U^E}\cot\left(\frac{U^E a}{2}\right) = +\frac{\varepsilon^\pm}{W^E} \tag{S66}$$

for the anti-symmetric electric mode, and

$$\frac{\varepsilon^m}{U^E}\tan\left(\frac{U^E a}{2}\right) = -\frac{\varepsilon^\pm}{W^E} \tag{S67}$$

for the symmetric electric mode, and

$$\frac{\mu^m}{U^H}\cot\left(\frac{U^H a}{2}\right) = +\frac{\mu^\pm}{W^H} \tag{S68}$$

for the anti-symmetric magnetic mode, and

$$\frac{\mu^m}{U^H}\tan\left(\frac{U^H a}{2}\right) = -\frac{\mu^\pm}{W^H} \tag{S69}$$

for the symmetric magnetic mode. Here, the parameters U^E, W^E, U^H and W^H can be expressed as

$$\begin{aligned} W^{E2} &= \beta^{E2} - k^{\pm 2} \quad W^{H2} = \beta^{H2} - k^{\pm 2} \\ U^{E2} &= k^{m2} - \beta^{E2} \quad U^{H2} = k^{m2} - \beta^{H2} \end{aligned}. \tag{S70}$$

Table S3. Electric/Magnetic field components of the **waveguide** modes

	$z > +\frac{a}{2}$	$-\frac{a}{2} < z < +\frac{a}{2}$	$z < -\frac{a}{2}$
E_x	$+C^{E+}\left(-\frac{W^E}{\beta^{E2}}\right)\frac{\partial\xi^E}{\partial x}e^{-W^E z}$ $+C^{H+}\frac{i\omega\mu^+}{\beta^{H2}}\frac{\partial\xi^H}{\partial y}e^{-W^H z}$	$+A^{Em}\left(+\frac{iU^E}{\beta^{E2}}\right)\frac{\partial\xi^E}{\partial x}e^{+iU^E z} + A^{Hm}\frac{i\omega\mu^m}{\beta^{H2}}\frac{\partial\xi^H}{\partial y}e^{+iU^H z}$ $+B^{Em}\left(-\frac{iU^E}{\beta^{E2}}\right)\frac{\partial\xi^E}{\partial x}e^{-iU^E z} + B^{Hm}\frac{i\omega\mu^m}{\beta^{H2}}\frac{\partial\xi^H}{\partial y}e^{-iU^H z}$	$+D^{E-}\left(-\frac{W^E}{\beta^{E2}}\right)\frac{\partial\xi^E}{\partial r}e^{+W^E z}$ $+D^{H-}\frac{i\omega\mu^-}{\beta^{H2}}\frac{\partial\xi^H}{\partial y}e^{+W^H z}$
E_y	$+C^{E+}\left(-\frac{W^E}{\beta^{E2}}\right)\frac{\partial\xi^E}{\partial y}e^{-W^E z}$ $-C^{H+}\frac{i\omega\mu^+}{\beta^{H2}}\frac{\partial\xi^H}{\partial x}e^{-W^H z}$	$+A^{Em}\left(+\frac{iU^E}{\beta^{E2}}\right)\frac{\partial\xi^E}{\partial y}e^{+iU^E z} - A^{Hm}\frac{i\omega\mu^m}{\beta^{H2}}\frac{\partial\xi^H}{\partial x}e^{+iU^H z}$ $+B^{Em}\left(-\frac{iU^E}{\beta^{E2}}\right)\frac{\partial\xi^E}{\partial y}e^{-iU^E z} - B^{Hm}\frac{i\omega\mu^m}{\beta^{H2}}\frac{\partial\xi^H}{\partial x}e^{-iU^H z}$	$+D^{E-}\left(-\frac{W^E}{\beta^{E2}}\right)\frac{\partial\xi^E}{\partial y}e^{+W^E z}$ $-D^{H-}\frac{i\omega\mu^-}{\beta^{H2}}\frac{\partial\xi^H}{\partial x}e^{+W^H z}$
E_z	$C^{E+}\xi^E e^{-W^E z}$	$A^{Em}\xi^E e^{+iU^E z} + B^{Em}\xi^E e^{-iU^E z}$	$D^{E-}\xi^E e^{+W^E z}$
H_x	$-C^{E+}\frac{i\omega\varepsilon^+}{\beta^{E2}}\frac{\partial\xi^E}{\partial y}e^{-W^E z}$ $+C^{H+}\left(-\frac{W^H}{\beta^{H2}}\right)\frac{\partial\xi^H}{\partial x}e^{-W^H z}$	$-A^{Em}\frac{i\omega\varepsilon^m}{\beta^{E2}}\frac{\partial\xi^E}{\partial y}e^{+iU^E z} + A^{Hm}\left(+\frac{iU^H}{\beta^{H2}}\right)\frac{\partial\xi^H}{\partial x}e^{+iU^H z}$ $-B^{Em}\frac{i\omega\varepsilon^m}{\beta^{E2}}\frac{\partial\xi^E}{\partial y}e^{-iU^E z} + B^{Hm}\left(-\frac{iU^H}{\beta^{H2}}\right)\frac{\partial\xi^H}{\partial x}e^{-iU^H z}$	$-D^{E-}\frac{i\omega\varepsilon^-}{\beta^{E2}}\frac{\partial\xi^E}{\partial y}e^{+W^E z}$ $+D^{H-}\left(-\frac{W^H}{\beta^{H2}}\right)\frac{\partial\xi^H}{\partial x}e^{+W^H z}$
H_y	$+C^{E+}\frac{i\omega\varepsilon^+}{\beta^{E2}}\frac{\partial\xi^E}{\partial x}e^{-W^E z}$ $+C^{H+}\left(-\frac{W^H}{\beta^{H2}}\right)\frac{\partial\xi^H}{\partial y}e^{-W^H z}$	$+A^{Em}\frac{i\omega\varepsilon^m}{\beta^{E2}}\frac{\partial\xi^E}{\partial x}e^{+iU^E z} + A^{Hm}\left(+\frac{iU^H}{\beta^{H2}}\right)\frac{\partial\xi^H}{\partial y}e^{+iU^H z}$ $+B^{Em}\frac{i\omega\varepsilon^m}{\beta^{E2}}\frac{\partial\xi^E}{\partial x}e^{-iU^E z} + B^{Hm}\left(-\frac{iU^H}{\beta^{H2}}\right)\frac{\partial\xi^H}{\partial y}e^{-iU^H z}$	$+D^{E-}\frac{i\omega\varepsilon^-}{\beta^{E2}}\frac{\partial\xi^E}{\partial x}e^{+W^E z}$ $+D^{H-}\left(-\frac{W^H}{\beta^{H2}}\right)\frac{\partial\xi^H}{\partial y}e^{+W^H z}$
H_z	$C^{H+}\xi^H e^{-W^H z}$	$A^{Hm}\xi^H e^{+iU^H z} + B^{Hm}\xi^H e^{-iU^H z}$	$D^{H-}\xi^H e^{+W^H z}$

By solving the propagation constants β^E and β^H (pure real numbers), the field parameters for the symmetric modes are

$$\begin{aligned} A^{Em} &= B^{Em} \quad C^{E+} = D^{E-} \quad A^{Em} = C^{E+}\frac{\varepsilon^\pm}{\varepsilon^m}\exp\left(-\frac{W^E a}{2}\right)\Big/\left[\exp\left(+i\frac{U^E a}{2}\right) + \exp\left(-i\frac{U^E a}{2}\right)\right] \\ A^{Hm} &= B^{Hm} \quad C^{H+} = D^{H-} \quad A^{Hm} = C^{H+}\frac{\mu^\pm}{\mu^m}\exp\left(-\frac{W^H a}{2}\right)\Big/\left[\exp\left(+\frac{iU^H a}{2}\right) + \exp\left(-\frac{iU^H a}{2}\right)\right] \end{aligned}. \tag{S71}$$

Moreover, the field parameters for the anti-symmetric modes are

$$\begin{aligned} A^{Em} &= +B^{Em} \quad C^{E+} = -D^{E-} \quad A^{Em} = C^{E+}\frac{\varepsilon^\pm}{\varepsilon^m}\exp\left(-\frac{W^E a}{2}\right)\Big/\left[\exp\left(+i\frac{U^E a}{2}\right) - \exp\left(-i\frac{U^E a}{2}\right)\right] \\ A^{Hm} &= +B^{Hm} \quad C^{H+} = -D^{H-} \quad A^{Hm} = C^{H+}\frac{\mu^\pm}{\mu^m}\exp\left(-\frac{W^H a}{2}\right)\Big/\left[\exp\left(+\frac{iU^H a}{2}\right) - \exp\left(-\frac{iU^H a}{2}\right)\right] \end{aligned}. \tag{S72}$$

Since only the relative amplitude makes physical sense, one can set A^{Hm} to be 1 and $A^{Em} = \pm i\sqrt{\mu_0/\varepsilon_0}$, and then the field distributions excited by circularly polarized light can be calculated properly. The dispersion relations of the symmetric (red/magenta) and antisymmetric (blue/green) magnetic/electric modes are shown in **Fig. S8(b-c)**, respectively.

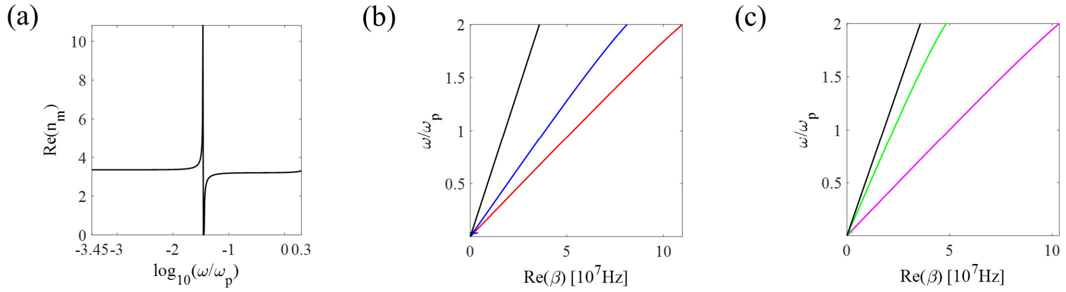

Fig. S8. Dispersive relations of waveguide modes at air-dielectric-air structure. (a) the relative permittivity of dielectric via the frequency; (b) the propagating constants of symmetric (red line) and anti-symmetric (blue line) magnetic modes via the frequency and (c) the propagating constants of symmetric (magenta line) and anti-symmetric (green line) electric modes via the frequency. Here, we only focus on the frequency with refractive index larger than 1. And the relative permittivity is $n^2 = 9 + \frac{\frac{A_1}{B_1}4\pi^2c^2}{\frac{1}{B_1}4\pi^2c^2-\omega^2} + \frac{\frac{A_2}{B_2}4\pi^2c^2}{\frac{1}{B_2}4\pi^2c^2-\omega^2} + \frac{\frac{A_3}{B_3}4\pi^2c^2}{\frac{1}{B_3}4\pi^2c^2-\omega^2}$, where A_1=1.03961212, B_1=0.00600069867, A_2=0.231792344, B_2=0.0200179144, A_3=1.01046945 and B_3=103.560653.

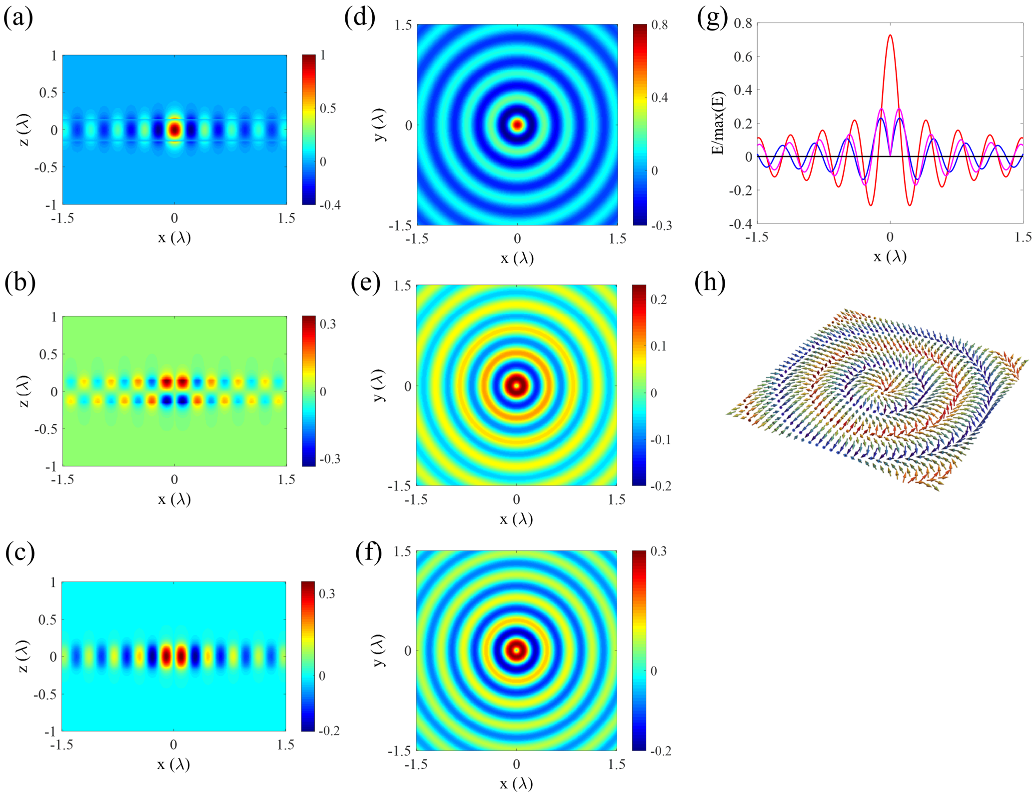

Fig. S9. Electric field defect constructed by the 0-order Bessel-type guided wave mode. The imaginary parts of (a) *z*-, (b) radial and (c) azimuthal electric field components in *xz*-plane ($y = 0$). In the layer, the imaginary parts of (d) *z*-, (e) radial and (f) azimuthal electric field components in *xy*-plane ($z = a/2 - 10$nm), and the corresponding (g) 1D contour at $y = 0$ and (h) electric field texture (region: $1.2\lambda\times1.2\lambda$). One can find that the electric field vector whirls from 'up' state to 'down' state along the radial and azimuthal direction simultaneously, which is a manifestation of twisted-type topological texture. Here, $\lambda = 9.90\times10^{-7}m$, which is corresponding to the angular frequency $\omega = 1.90\times10^{15}/s$. *a* is the thickness of metal and here we set $a = 0.3\lambda$.

In the case, the propagating constants of symmetric and anti-symmetric electric/magnetic modes are different completely. In the layer, the radial and azimuthal electric field components exist simultaneously for the 0-order Bessel-type mode, which is a manifestation of twisted-type field textures (**Fig. S9(d-h)**). The skyrmion number of electric field skyrmion lattice constructed by this waveguide mode can be -1, as shown in **Fig. 3(d)** in the main text. Noteworthily, owing to the boundary condition from Maxwell's equations, the normal electric field components are parallel and the horizontal electric field components are continuous through the interface (**Fig. S9**).

V. EM spin topological defects and their topological state transitions

In the section VI, we analyze the mode properties and electric field topological textures in multilayered structure. The formations of various configurations of field topological textures are based on the modes' coupling but not the SOCs. On the other hand, to understand the formations of various photonic spin topological defects in multilayered structures, we should analyze the SOC terms given in the Section II. Noteworthily, the dispersive effect is not considered in SOC terms (Eq. (S29) and Eq. (S31)) [28,56].

In the layer, the real and imaginary parts of SOC term are given by the gradient of helical density and vorticites of kinetic Abraham-Poynting momentum. The expressions of gradient helical density are

$$\left(\mathrm{Re}\,\mathbf{H}_{\mathrm{SO}}\right)_r=-\frac{\hbar\omega}{k^2}\left(\nabla C\right)_r=\frac{\hbar}{2}\mathrm{Im}\left\{\frac{\partial E_z^*}{\partial r}H_z+E_z^*\frac{\partial H_z}{\partial r}+\frac{\partial E_r^*}{\partial r}H_r+E_r^*\frac{\partial H_r}{\partial r}+\frac{\partial E_\varphi^*}{\partial r}H_\varphi+E_\varphi^*\frac{\partial H_\varphi}{\partial r}\right\}, \tag{S73}$$

$$\left(\mathrm{Re}\,\mathbf{H}_{\mathrm{SO}}\right)_\varphi=-\frac{\hbar\omega}{k^2}\left(\nabla C\right)_\varphi=0\,, \tag{S74}$$

and

$$\left(\mathrm{Re}\,\mathbf{H}_{\mathrm{SO}}\right)_z=-\frac{\hbar\omega}{k^2}\left(\nabla C\right)_z=\frac{\hbar}{2}\mathrm{Im}\left\{\frac{\partial E_z^*}{\partial z}H_z+E_z^*\frac{\partial H_z}{\partial z}+\frac{\partial E_r^*}{\partial z}H_r+E_r^*\frac{\partial H_r}{\partial z}+\frac{\partial E_\varphi^*}{\partial z}H_\varphi+E_\varphi^*\frac{\partial H_\varphi}{\partial z}\right\}. \tag{S75}$$

And the vorticites of kinetic Abraham-Poynting momentum are

$$\left(\mathrm{Im}\,\mathbf{H}_{\mathrm{SO}}\right)_r=\frac{\hbar}{2}\left(\nabla\times\mathbf{p}^A\right)_r=-\frac{\hbar}{2}\frac{\partial p_\varphi^A}{\partial z}=\frac{\hbar}{4}\mathrm{Re}\left\{-\frac{\partial E_z^*}{\partial z}H_r-E_z^*\frac{\partial H_r}{\partial z}+\frac{\partial E_r^*}{\partial z}H_z+E_r^*\frac{\partial H_z}{\partial z}\right\}, \tag{S76}$$

$$\left(\mathrm{Im}\,\mathbf{H}_{\mathrm{SO}}\right)_\varphi=\frac{\hbar}{2}\left(\nabla\times\mathbf{p}^A\right)_\varphi=\frac{\hbar}{2}\left(\frac{\partial p_r^A}{\partial z}-\frac{\partial p_z^A}{\partial r}\right)=\frac{\hbar}{4}\mathrm{Re}\left\{\begin{array}{l}\dfrac{\partial E_\varphi^*}{\partial z}H_z+E_\varphi^*\dfrac{\partial H_z}{\partial z}-\dfrac{\partial E_z^*}{\partial z}H_\varphi-E_z^*\dfrac{\partial H_\varphi}{\partial z}\\-\dfrac{\partial E_r^*}{\partial r}H_\varphi-E_r^*\dfrac{\partial H_\varphi}{\partial r}+\dfrac{\partial E_\varphi^*}{\partial r}H_r+E_\varphi^*\dfrac{\partial H_r}{\partial r}\end{array}\right\}, \tag{S77}$$

$$\left(\mathrm{Im}\,\mathbf{H}_{\mathrm{SO}}\right)_z=\frac{\hbar}{2}\left(\nabla\times\mathbf{p}^A\right)_z=\frac{\hbar}{2}\frac{1}{r}\frac{\partial rp_\varphi^A}{\partial r}=\frac{\hbar}{4}\mathrm{Re}\left\{\frac{\partial E_z^*}{\partial r}H_r+E_z^*\frac{\partial H_r}{\partial r}-\frac{\partial E_r^*}{\partial r}H_z-E_r^*\frac{\partial H_z}{\partial r}+\frac{E_z^*H_r-E_r^*H_z}{r}\right\}. \tag{S78}$$

For the real part of SOC term, the variation of EM helicity is corresponding to the variation of longitudinal spin, because the longitudinal spin is proportional to the EM helicity by $\mathbf{S}_l=\sum\hbar\sigma_h\hat{\mathbf{k}}$ [57]. The variation of longitudinal spin is widely existing in the phenomena of spin-orbit interactions such as: the spin-based position of light and the spin-based orbital angular momentum of light [43,44]. Whereas the vorticities of kinetic Abraham-Poynting momentum is corresponding to the EM transverse spin [23,57,58], which is related to the structural properties of EM fields. Moreover, the EM transverse spin given by the vorticities of kinetic Abraham-Poynting momentum also represents the intrinsic spin-momentum locking of light [60], and is widely existing in the phenomena of spin-orbit interactions such as: unidirectional guided wave of light [36-38], orbital-to-spin AM conversions [43] and photonic spin topological defects [19,21-28]. Particularly, in section III, we demonstrate that either the Néel-type or the Bloch-type or the twisted-type skyrmions can be excited in the confined EM field, and the point that determines which one would be generated is the SOC terms given by Eqs. (S73-S78).

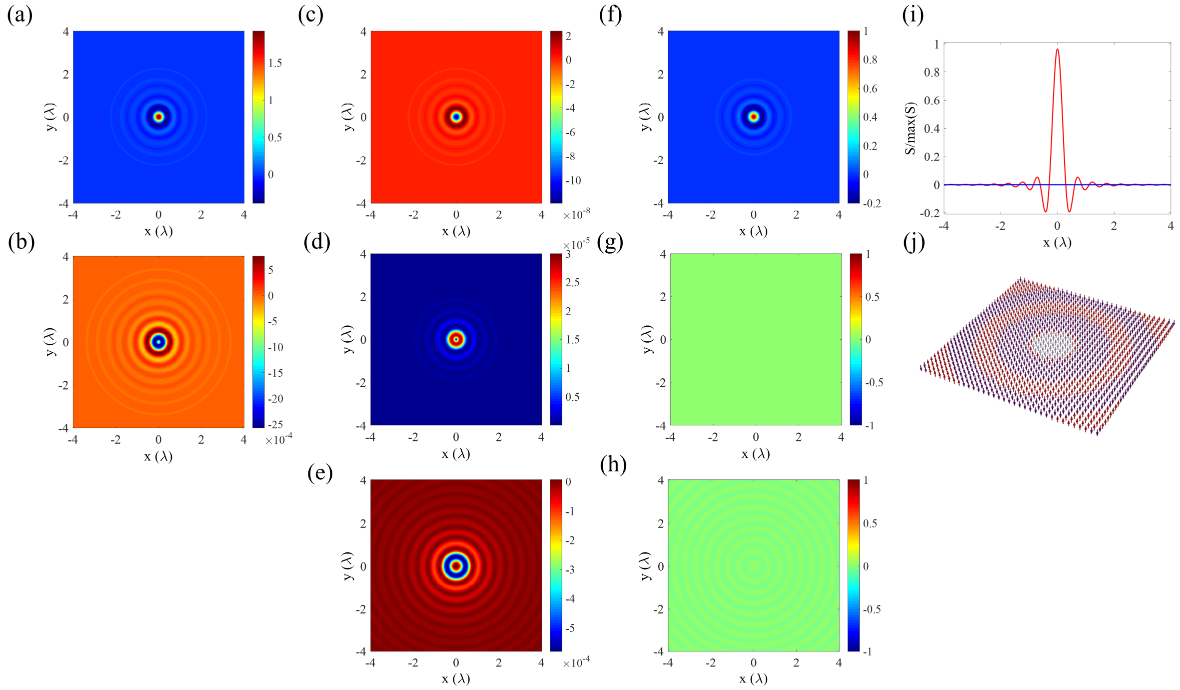

Fig. S10. SOC and spin texture of +1-order Bessel-type surface mode at a low frequency limit. In the metal layer, the (a) z- and (b) radial components of real part of SOC term Re$\mathbf{H}_{\mathrm{SO}}$ in xy-plane ($z = a/2 - 10$nm). The (c) z-, (d) radial and (e) azimuthal components of imaginary part of SOC term Im$\mathbf{H}_{\mathrm{SO}}$ in xy-plane ($z = a/2 - 10$nm). The (f) z-, (g) radial and (h) azimuthal SAM components in xy-plane ($z = a/2 - 10$nm), and the corresponding (i) 1D contour at $y = 0$ and (j) spin texture (region: $2\lambda\times2\lambda$). One can find that the amplitude of z-component SAM is much larger that of horizontal SAM components, and a cylindrical domain wall-like texture (skyrmion number $N_{SK} = -1$) is present. Here, $\lambda = 1\times10^{-3}m$, which is corresponding to the angular frequency $\omega = 1.88\times10^{12}/s$. a is the thickness of metal and here we set $a = 0.2\lambda$.

For the SPP modes in the air-metal-air multilayered structure, if the frequency is small enough ($\omega << \omega_p$, such as terahertz wave), there is $1 + \varepsilon^m/\varepsilon_0 \approx \varepsilon^m/\varepsilon_0$ and thus the propagating constant $\beta \approx k^{\pm} = k_0$ is a pure real number approximatively, as indicated by region **I** in **Fig. 1(a)**. In the case, the decaying factor in the metal is enormous because $k_z^m = \sqrt{\beta^2 - (k^m)^2} \gg \beta$ and the EM field is only localized in the surface of conductor. Therefore, the real part of the z-component of SOC term (Re$\mathbf{H}_{\mathrm{SO}}$)$_z$ is much larger than the real part of the horizontal components of SOC term (Re$\mathbf{H}_{\mathrm{SO}}$)$_r$ (**Fig. S10(a-b)**). In addition, the imaginary parts of SOC term (Im$\mathbf{H}_{\mathrm{SO}}$) will affect the horizontal SAMs by two mechanisms: 1. Rashba-like SOC leading to radial SAM by $\left(\hat{\mathbf{n}} \times P_\varphi^A\right) \cdot \mathbf{S}$, which is also corresponding to the intrinsic spin-momentum locking of EM wave [60]; 2. Azimuthal SAM originating from the z-component kinetic Abraham-Poynting momentum by $(\nabla_r \times P_z^A)$ [58]. The configuration of photonic spin topological defects is determined by the ratio of these two mechanisms. In the instance, the magnitude of z-

component kinetic Abraham-Poynting momentum is larger than that of azimuthal kinetic Abraham-Poynting momentum, and thus the magnitude of azimuthal EM transverse spin is larger than that of radial EM transverse spin. However, both two the horizontal SAMs are extremely small (**Fig. S10(c-e)**). Thus, it can be considered that there is only the SOC in the z-direction, which results in the z-component SAM being prominent (**Fig. S10(f-h)**). Particularly at a low frequency limit, and the spin topological textures of +1-order Bessel-type surface modes can be considered as a combination of purely 'up' state and 'down' state universally (**Figs. S10(i-j)**).

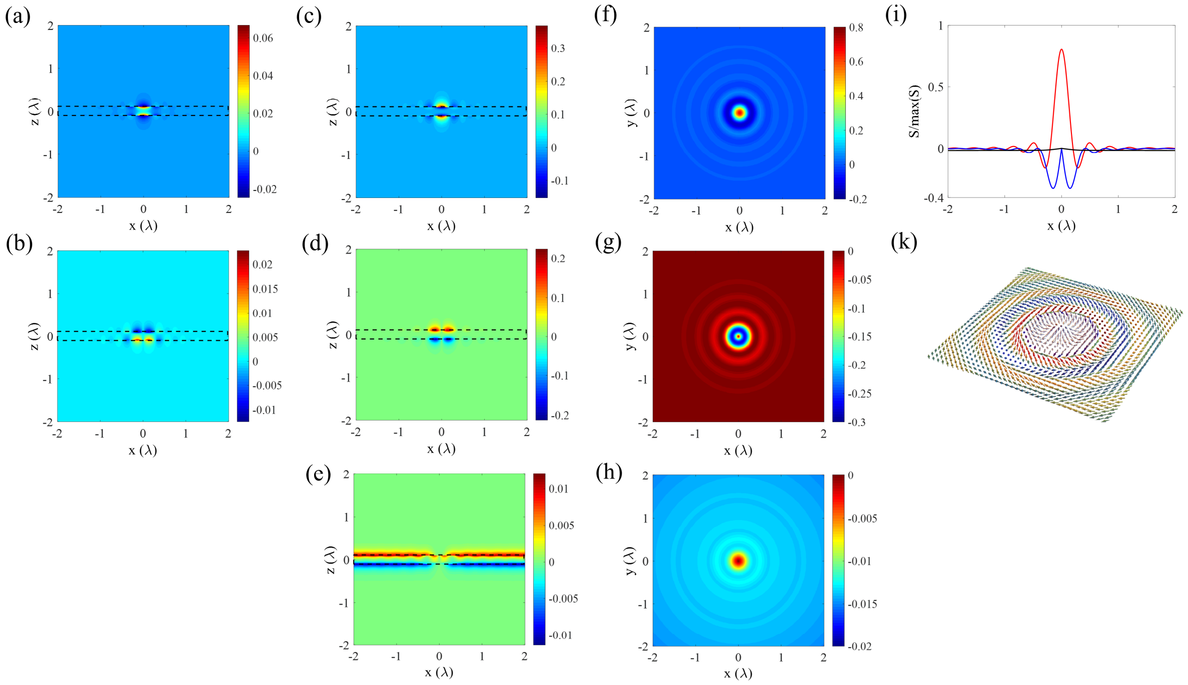

Fig. S11. SOC and spin texture of +1-order Bessel-type surface mode at visible frequency. In the metal layer, the (a) z- and (b) radial components of real part of SOC term Re$\mathbf{H}_{SO}$ in xz-plane ($y = 0$). The (c) z-, (d) radial and (e) azimuthal components of imaginary part of SOC term Im$\mathbf{H}_{SO}$ in xz-plane ($y = 0$). The (f) z-, (g) radial and (h) azimuthal spin components in xy-plane ($z = a/2 - 10$nm), and the corresponding (i) 1D contour at $y = 0$ and (j) spin texture (region: $2\lambda\times2\lambda$). One can find that the spin vectors vary from 'up' state to 'down' state in a period, and thus the skyrmion number $N_{SK} = -1$. However, since an azimuthal spin component exists, it is a manifestation of twisted-type skyrmion texture. This twisted-type skyrmion can be also found in the hyperbolic Metamaterials [S4]. Here, $\lambda = 6.38\times10^{-7}m$, which is corresponding to the angular frequency $\omega = 2.95\times10^{15}/s$. a is the thickness of metal and here we set $a = 0.2\lambda$.

As the frequency increases (for example, in the near-infrared or visible spectrum), the propagating constant is a complex number and Re(β) > k_0 owing to the fact that Re($\varepsilon^m/\varepsilon_0$) < Re($1+\varepsilon^m/\varepsilon_0$) < 0, as indicated by region **II** in **Fig. 1(a)**. In the case, the z-component wavenumber $k_z^m = \sqrt{\beta^2 - (k^m)^2}$ has a same order of magnitudes with the propagating constant β. Thus, the real and imaginary parts of the z-component SOC term are nonzero ((Re$\mathbf{H}_{SO}$)$_z$ in **Fig. S11(a)** and (Im$\mathbf{H}_{SO}$)$_z$ in **Fig. S11(c)**) and lead to the z-component SAM (**Fig. S11(f)**). In addition, the SOC in the z-direction (**Fig. S11(d)**) results in the radial SAM by $\left(\hat{\mathbf{n}} \times P_\varphi^A\right) \cdot \mathbf{S}$ (**Fig. S11(g)**). On the other hand, owing to the complex property of propagation constant or the lossy property of these EM modes, the kinetic Abraham-Poynting momentum in the z-direction appears, and thus the azimuthal SAM component appears since $S_\varphi \propto (\nabla_r \times P_z^A)$ (**Fig. S11(e)**) and thus the spin textures can be considered as the twisted-type skyrmions (skyrmion number $N_{SK} = \pm1$) (**Fig. S11(i-k)**). Noteworthily, owing to the intrinsic spin-momentum locking of EM field in dispersive medium, the dispersion will cause that the spin-momentum locking is transformed from right hand rule to left hand rule [28], and thus the signs of SAMs in **Fig. S11(c)**/**Fig. S11(d)** and **Fig. S11(f)**/**Fig. S11(g)** are opposite.

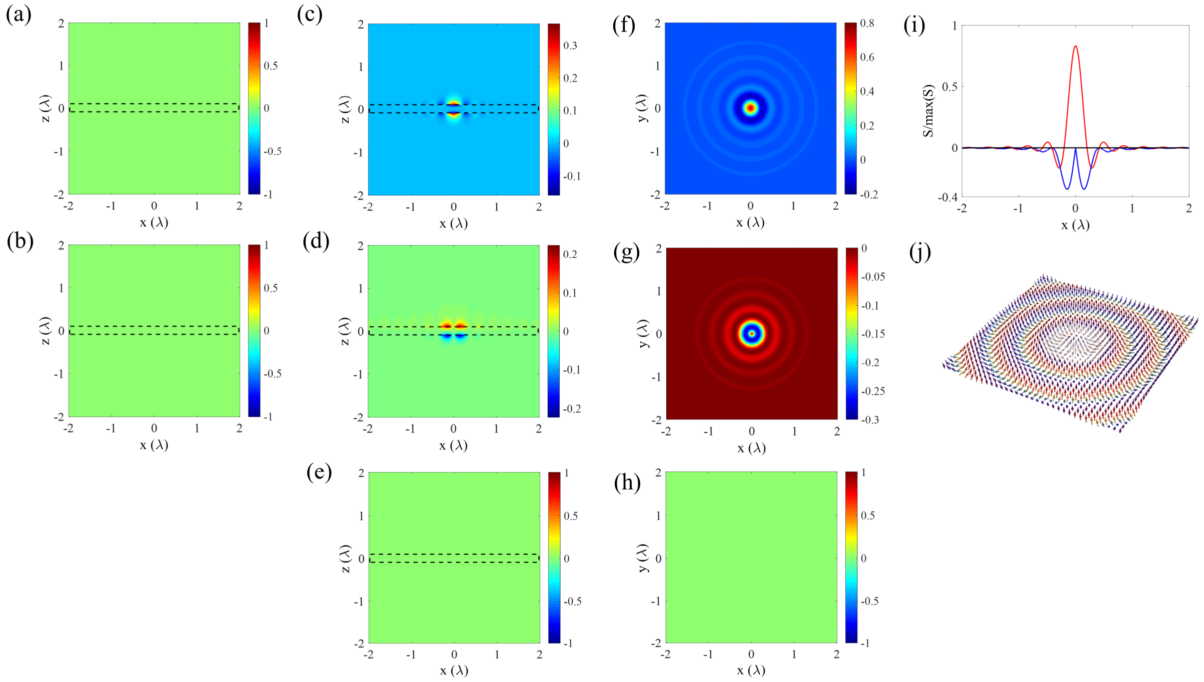

Fig. S12. SOC and spin texture of +1-order Bessel-type surface mode at lossless limit. In the metal layer, the (a) z- and (b) radial components of real part of SOC term Re$\mathbf{H}_{\mathrm{SO}}$ in xz-plane (y = 0). The (c) z-, (d) radial and (e) azimuthal components of imaginary part of SOC term Im$\mathbf{H}_{\mathrm{SO}}$ in xz-plane (y = 0). The (f) z-, (g) radial and (h) azimuthal spin components in xy-plane ($z = a/2 - 10$nm), and the corresponding (i) 1D contour at y = 0 and (j) spin texture (region: $2\lambda\times2\lambda$). One can find that, in a period, the spin vectors vary from 'up' state to 'down' state, and thus the skyrmion number $N_{SK} = -1$. The azimuthal spin component is zero in the case, which is a manifestation of Néel-type skyrmion texture. Here, $\gamma = 0$, $\lambda = 6.38\times10^{-7}m$, which is corresponding to the angular frequency $\omega = 2.95\times10^{15}/s$. a is the thickness of metal and here we set $a = 0.2\lambda$.

At the lossless limit, as shown in region **III** of **Fig. 1(a)**, the helical density is zero and the gradient of helical density is also zero (Re$\mathbf{H}_{\mathrm{SO}}$ = 0) (**Fig. S12(a-b)**). However, the z component of the imaginary part of SOC term (Im$\mathbf{H}_{\mathrm{SO}}$)$_z$ is nonzero (**Fig. S12(c)**). Thus, there is still the z-component SAM. On the other hand, there is only azimuthal kinetic Abraham-Poynting momentum in the layer and thus the azimuthal component of imaginary SOC term disappears (**Fig. S12(d-e)**). Therefore, the configuration of spin topological defect is translated from the twisted type to Néel-type (**Figs. S11(f-j)**). From the intrinsic spin-momentum locking property of EM field in dispersive medium [28], the spin-momentum locking is transformed from right hand rule to left hand rule, and thus the signs of SAMs in **Fig. S12(c)**/**Fig. S12(d)** and **Fig. S12(f)**/**Fig. S12(g)** are opposite.

In the part **IV** of **Fig. 1(a)**, the propagating constant β is a pure imaginary number and the propagating mode is forbidden. Thus, no spin topological defect exists in the situation.

As the frequency increases larger than the plasma frequency $\omega > \omega_p$, the metal is transformed to dielectric with relative permittivity smaller than 1. The slot-waveguide-like mode will be present in the layer and the propagation constant is localized beyond the light cone comparing to that of SPP modes (within the light cone), as shown in region **V** of **Fig. 1(a)**. The propagation constant is purely real and equal to the wave number in the medium layer approximatively. Therefore, the decaying factor in the z-direction is extremely small and one can consider that the helical density is homogeneous in the layer along the *z*-direction, which causes that the *z*-component of real part of SOC term is zero in the layer $(\mathrm{Re}\mathbf{H}_{\mathrm{SO}})_z = 0$. Thus, the *z*-component SAM is determined by the imaginary part of the SOC term $(\mathrm{Im}\mathbf{H}_{\mathrm{SO}})_z$. In the case, the kinetic Abraham-Poynting momentum in the *z*-component is nonzero, and the azimuthal SAM appears due to $S_\varphi \propto (\nabla_r \times P_z^A)$ (**Fig. S13(e)**). On the other hand, the radial SAM is given by $\left(\hat{\mathbf{n}} \times P_\varphi^A\right) \cdot \mathbf{S}$. Because the outer normal direction of upper interface is inverse to that of the lower interface whereas the azimuthal kinetic Abraham-Poynting momenta are parallel in the upper and lower interfaces, the radial SAM is cancelled out in the layer (**Fig. S13(g)**). This is a manifestation of Bloch-type spin topological defect (**Fig. S13(i-j)**). Moreover, the Bloch-type configuration is stable through the layer, which is one of key achievement of our manuscript. Noteworthily, since the relative permittivity of layer is larger than 0, the intrinsic spin-momentum locking satisfies the right hand rule in the layer, and the sign of SOC term in **Fig. S13(c)/Fig. S13(e)** is consistent with that of SAM in **Fig. S13(f)/Fig. S13(h)**.

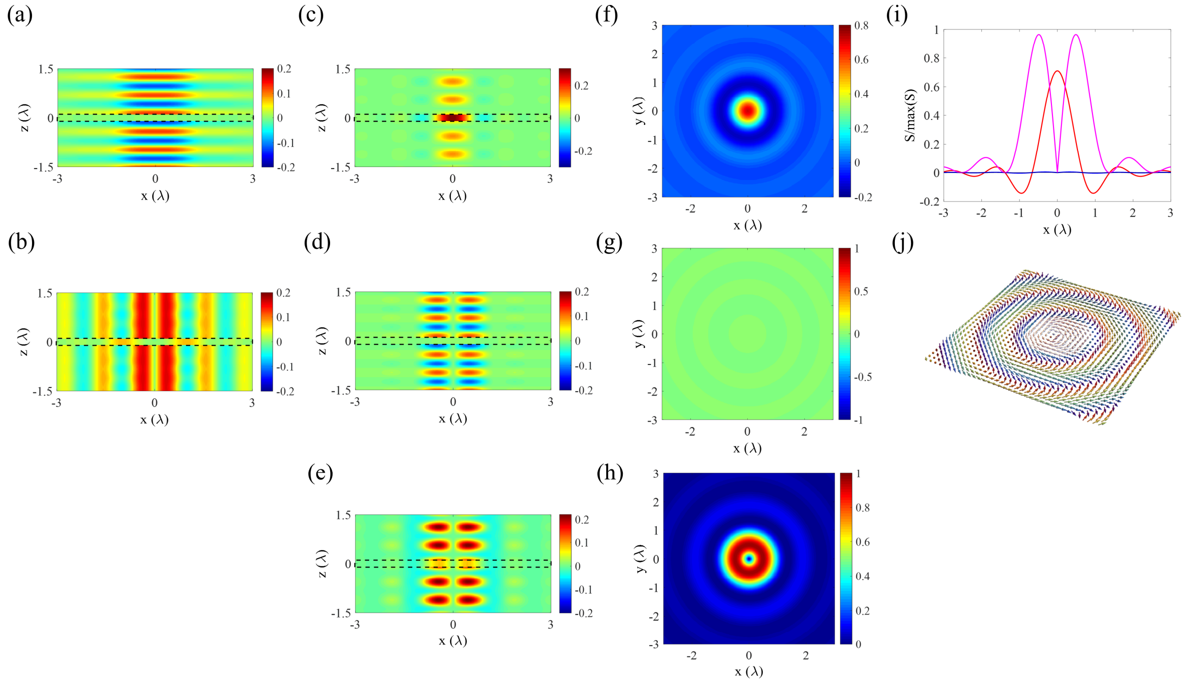

Fig. S13. SOC and spin defect of +1-order Bessel-type surface mode at frequency larger than the plasma frequency. In the layer, the (a) *z*- and (b) radial components of real part of SOC term $\mathrm{Re}\mathbf{H}_{\mathrm{SO}}$ in *xz*-plane ($y = 0$). The (c) *z*-, (d) radial and (e) azimuthal components of imaginary part of SOC term $\mathrm{Im}\mathbf{H}_{\mathrm{SO}}$ in *xz*-plane ($y = 0$). The (f) *z*-, (g) radial and (h) azimuthal spin components in *xy*-plane ($z = 0$), and the corresponding (i) 1D contour at $y = 0$ and (j) spin texture (region: $8\lambda\times8\lambda$). In the case, the slot-waveguide-like modes are present, and the symmetric TE and TM modes with their propagating constants identical are excited. The radial SAM component is cancelled out due to the intrinsic spin-momentum locking property of EM transverse spins in the upper and lower interfaces, which is a manifestation of Bloch-type topological texture. In a period, the spin vectors vary from 'up' state to 'down' state, and thus the skyrmion number $N_{SK} = -1$. Here, $\lambda = 3.33\times10^{-7}m$, which is corresponding to the angular frequency $\omega = 5.66\times10^{15}/s$. *a* is the thickness of metal and here we set $a = 0.2\lambda$.

For the waveguide mode in **Fig 2(a)**, the *z*-component and radial component of gradient helical density (**Fig. S14(a-b)**) and the three components of vorticities of kinetic Abraham-Poynting momentum (**Fig. S14(c-e)**) appear simultaneously (the *z*-component kinetic Abraham-Poynting momentum is nonzero). Thus, the radial and azimuthal SAM components are existing simultaneously (**Fig. S14(f-h)**) in the layer for the +1-order Bessel-type mode, which is a manifestation of twisted-type spin topological textures (**Fig. S14(i-j)**).

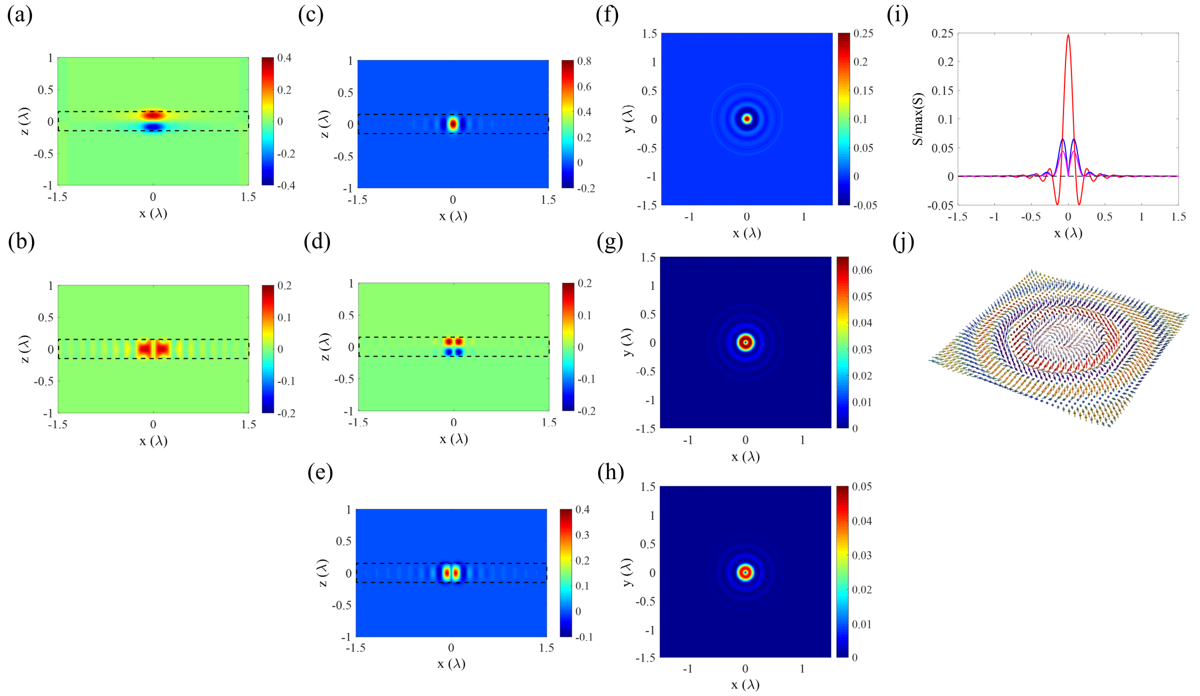

Fig. S14. SOC and spin defect of +1-order Bessel-type surface mode at visible frequency. In the layer, the (a) *z*- and (b) radial components of real part of SOC term Re$\mathbf{H}_{SO}$ in *xz*-plane ($y = 0$). The (c) *z*-, (d) radial and (e) azimuthal components of imaginary part of SOC term Im$\mathbf{H}_{SO}$ in *xz*-plane ($y = 0$). The (f) *z*-, (g) radial and (h) azimuthal spin components in *xy*-plane ($z = a/2 - 10\text{nm}$), and the corresponding (i) 1D contour at $y = 0$ and (j) spin texture (region: $\lambda\times\lambda$). In a period, the twisted-type spin textures vary from 'up' state to 'down' state. Thus, the skyrmion number is −1 ($N_{SK} = -1$). Here, $\lambda = 9.90\times10^{-7}m$, which is corresponding to the angular frequency $\omega = 1.90\times10^{15}/s$. *a* is the thickness of metal and here we set $a = 0.3\lambda$.

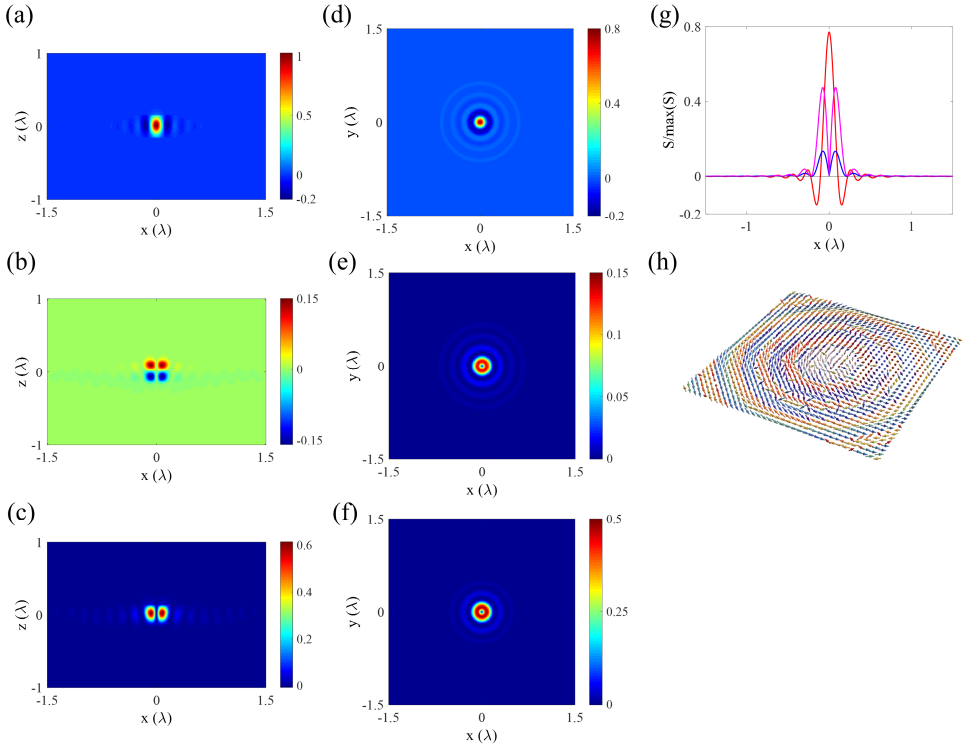

Fig. S15. Spin defect of hybrid modes containing the symmetric and antisymmetric +1-order Bessel-type guided wave modes at visible frequency. The (a) *z*-, (b) radial and (c) azimuthal SAM components in *xz*-plane ($y = 0$). In the layer, the (d) *z*-, (e) radial and (f) azimuthal spin components in *xy*-plane ($z = a/2 - 10\text{nm}$), and the corresponding (g) 1D contour at $y = 0$ and (h) spin texture (region: $1.2\lambda\times1.2\lambda$). It can be observed that the skyrmion numbers are unequal to ±1 ($N_{SK} \neq \pm1$) owing to the mismatch of propagating constants between the symmetric and antisymmetric guided modes, which indicates a topological phase transition. Here, $\lambda = 9.90\times10^{-7}m$, which is corresponding to the angular frequency $\omega = 1.90\times10^{15}/s$. a is the thickness of metal and here we set $a = 0.3\lambda$.

In addition, it can be noticed that there will be the symmetric and antisymmetric modes existing for the EM modes within the light cone. When the modes are beyond the light cone ($v_{\text{ph}} > c$), only the symmetric modes exist in the structure. More importantly, the propagating constants of symmetric electric and magnetic modes are identical, and hence the topological geometry of the photonic topological textures constructed by these symmetric electric and magnetic EM modes are maintained from the modes' coupling. Whereas if the modes are localized within the light cone ($v_{\text{ph}} < c$), the propagating constants of symmetric and antisymmetric modes are different. In this instance, one cannot find a connected boundary to define the topological geometry of this spin texture constructed by the symmetric and antisymmetric EM modes simultaneously (**Fig. S15**). Therefore, we can conclude that the coupling between these symmetric and antisymmetric modes will result in a photonic analogy of topological phase transition for the spin texture.

VI. EM topological defects in C4 and C6 rotating symmetry

Here, we first give the details of derivations of field distributions for the photonic meron and skyrmion lattices in C4 and C6 rotating symmetries, respectively.

The normal electric field component $E_z = A/\varepsilon\beta^2\xi$ should fulfill the Helmholtz equation

$$\nabla_\perp^2\xi(x,y,z)+\beta^2\xi(x,y,z)=0\,, \tag{S79}$$

where the trial solution can be expressed as

$$\xi(x,y,z)=X(x)Y(y)e^{\pm k_z z}\,. \tag{S80}$$

Here, the $+k_z z$ indicates the field decay to the negative infinity (below the interface) while $-k_z z$ indicates the field decay to the positive infinity (above the interface). By substituting equation (S80) into equation (S79), it can be obtained that

$$\frac{1}{X}\frac{\partial^2 X}{\partial x^2}+\frac{1}{Y}\frac{\partial^2 Y}{\partial y^2}+\beta^2=0\,, \tag{S81}$$

which can be separated into

$$\begin{cases}\dfrac{1}{X}\dfrac{\partial^2 X}{\partial x^2}+u\beta^2=0\\[2mm] \dfrac{1}{Y}\dfrac{\partial^2 Y}{\partial y^2}+v\beta^2=0\end{cases} \tag{S82}$$

with $u + v = 1$. The nontrivial solution of expression (S79) is

$$\xi(x,y,z)=\begin{Bmatrix}A\sin\left(\sqrt{u}\beta x\right)\sin\left(\sqrt{v}\beta y\right)+B\cos\left(\sqrt{u}\beta x\right)\cos\left(\sqrt{v}\beta y\right)\\ +C\sin\left(\sqrt{u}\beta x\right)\cos\left(\sqrt{v}\beta y\right)+D\cos\left(\sqrt{u}\beta x\right)\sin\left(\sqrt{v}\beta y\right)\end{Bmatrix}e^{\pm k_z z}\,. \tag{S83}$$

If we set

$$\begin{aligned} L_x &= \frac{2n\pi}{\sqrt{u\beta}} = 2\lambda_{sp} \quad n = \text{integer} \\ L_y &= \frac{2m\pi}{\sqrt{v\beta}} = 2\lambda_{sp} \quad m = \text{integer} \end{aligned} \tag{S84}$$

with $\lambda_{sp}= 2\pi/\beta$, one can get

$$\mu+\nu=\left(\frac{2n\pi}{L_x\beta}\right)^2+\left(\frac{2m\pi}{L_y\beta}\right)^2=\lambda_{sp}^2\left[\left(\frac{n}{L_x}\right)^2+\left(\frac{m}{L_y}\right)^2\right]=\frac{1}{4}\left[n^2+m^2\right]=1\,, \tag{S85}$$

and then one can obtain that two groups of solutions

$$n=0 \quad m=\pm 2 \;\text{ and }\; n=\pm 2 \quad m=0\,. \tag{S86}$$

Therefore, the nontrivial solution in expression (S83) is converted into

$$\begin{aligned} \xi(x,y,z) &= \left\{A\cos(\beta x)+B\cos(\beta y)+C\sin(\pm\beta x)+D\sin(\pm\beta y)\right\}e^{\pm k_z z} \\ &= \left\{A'\cos(\beta x)+B'\cos(\beta y)+C'\sin(\beta x)+D'\sin(\beta y)\right\}e^{\pm k_z z} \end{aligned}\,. \tag{S87}$$

The parameters in expression (S87) can be calculated further with rotating symmetry with rotating matrix $R_z(\varphi)$. The rotating symmetry operator can be expressed as

$$R_z(\varphi)\left\{E_z\left[R_z(-\varphi)\vec{\mathbf{r}}\right]\hat{\mathbf{z}}\right\}=e^{il\varphi}\left\{E_z(\vec{\mathbf{r}})\hat{\mathbf{z}}\right\}. \tag{S88}$$

Note here that there is always $R_z(\varphi)\{E_z\hat{\mathbf{z}}\}=E_z\hat{\mathbf{z}}$ for the normal electric field component.

For the C4 rotational symmetry, the calculated *z*-component electric field components are given in **Table. S4**.

Table. S4. Calculated *z*-component electric field component for the meron lattices

$l=0$	$E_z=\frac{A_0}{\varepsilon}\xi=\frac{A_0}{\varepsilon}\left\{\cos(\beta x)+\cos(\beta y)\right\}e^{\pm k_z z}$
$l=1$	$E_z=\frac{A_1}{\varepsilon}\xi=\frac{A_1}{\varepsilon}\left\{\sin(\beta y)+i\sin(\beta x)\right\}e^{\pm k_z z}$
$l=2$	$E_z=\frac{A_2}{\varepsilon}\xi=\frac{A_2}{\varepsilon}\left\{\cos(\beta y)-\cos(\beta x)\right\}e^{\pm k_z z}$
$l=3$	$E_z=\frac{A_3}{\varepsilon}\xi=\frac{A_3}{\varepsilon}\left\{\sin(\beta y)-i\sin(\beta x)\right\}e^{\pm k_z z}$

As the l=0 or l=2, the spin-orbit coupling is absence in the cases, the electric field distributions can be regarded as the field meron lattices [26]. While for l=1 and l=3, the spin vectors can be regarded as the spin meron lattices [26]. Here, we only consider l = 1, where the skyrmion number of spin meron lattices is ±1/2.

For the C6 rotational symmetry, the calculated *z*-component electric field components are given in **Table. S5**. As the l=0 and l=3, the spin-orbit coupling is absence, the electric field distributions can be regarded as the field skyrmion lattices [18,20]. While for l=1, l=2, l=4 and l=5, the spin vectors can be regarded as the spin skyrmion lattices [26]. Here, we only consider l=0, where the skyrmion number of field skyrmion lattices is ±1.

Table. S5. Calculated *z*-component electric field component for the skyrmion lattices

$l=0$	$E_z=\frac{B_0}{\varepsilon}\xi=\frac{B_0}{\varepsilon}\left\{\cos(\beta x)+\cos\left(\frac{1}{2}\beta x+\frac{\sqrt{3}}{2}\beta y\right)+\cos\left(\frac{1}{2}\beta x-\frac{\sqrt{3}}{2}\beta y\right)\right\}e^{\pm k_z z}$
$l=1$	$E_z=\frac{B_1}{\varepsilon}\xi=\frac{B_1}{\varepsilon}\left\{\frac{2}{\sqrt{3}}\sin\left(\frac{1}{2}\beta x\right)\cos\left(\frac{\sqrt{3}}{2}\beta y\right)+2i\cos\left(\frac{1}{2}\beta x\right)\sin\left(\frac{\sqrt{3}}{2}\beta y\right)+\frac{2}{\sqrt{3}}\sin(\beta x)\right\}e^{\pm k_z z}$
$l=2$	$E_z=\frac{B_2}{\varepsilon}\xi=\frac{B_2}{\varepsilon}\left\{-2i\sin\left(\frac{1}{2}\beta x\right)\sin\left(\frac{\sqrt{3}}{2}\beta y\right)-\frac{2}{\sqrt{3}}\cos\left(\frac{1}{2}\beta x\right)\cos\left(\frac{\sqrt{3}}{2}\beta y\right)+\frac{2}{\sqrt{3}}\cos(\beta x)\right\}e^{\pm k_z z}$
$l=3$	$E_z=\frac{B_3}{\varepsilon}\xi=\frac{B_3}{\varepsilon}\left\{\sin(\beta x)-\sin\left(\frac{1}{2}\beta x+\frac{\sqrt{3}}{2}\beta y\right)-\sin\left(\frac{1}{2}\beta x-\frac{\sqrt{3}}{2}\beta y\right)\right\}e^{\pm k_z z}$
$l=4$	$E_z=\frac{B_4}{\varepsilon}\xi=\frac{B_4}{\varepsilon}\left\{2i\sin\left(\frac{1}{2}\beta x\right)\sin\left(\frac{\sqrt{3}}{2}\beta y\right)-\frac{2}{\sqrt{3}}\cos\left(\frac{1}{2}\beta x\right)\cos\left(\frac{\sqrt{3}}{2}\beta y\right)+\frac{2}{\sqrt{3}}\cos(\beta x)\right\}e^{\pm k_z z}$
$l=5$	$E_z=\frac{B_5}{\varepsilon}\xi=\frac{B_5}{\varepsilon}\left\{\frac{2}{\sqrt{3}}\sin\left(\frac{1}{2}\beta x\right)\cos\left(\frac{\sqrt{3}}{2}\beta y\right)-2i\cos\left(\frac{1}{2}\beta x\right)\sin\left(\frac{\sqrt{3}}{2}\beta y\right)+\frac{2}{\sqrt{3}}\sin(\beta x)\right\}e^{\pm k_z z}$

REFERENCES:

[S1] Landau, L. D., Lifshitz, E. M., and Pitaevskii, L. P. *Electrodynamics of Continuous Media* (Pergamon, Oxford, 1984).

[S2] Shi, P., Li, H., Du, L., and Yuan, X. Spin-momentum properties in the paraxial optical system, ACS Photonics (2022). DOI: 10.1021/acsphotonics.2c01535

[S3] Zayats, Anatoly V., Smolyaninov, Igor I., Maradudin, Alexei A. Nano-optics of surface plasmon polaritons, Phys. Rep. **408**(3–4), 131-314 (2005).

[S4] Gan, S., Shi, P., Yang, A., Lin, M., Du, L., and Yuan, X. Deep-subwavelength optical spin textures in volume plasmon polaritons with hyperbolic metamaterials, Adv. Optical Mater. **11**, 2201986 (2023).